





## FEATURE ARTICLE

# High-entropy oxides: Harnessing crystalline disorder for emergent functionality

George N. Kotsonis<sup>1</sup>  | Saeed S. I. Almishal<sup>1</sup>  | Francisco Marques dos Santos Vieira<sup>1</sup> | Vincent H. Crespi<sup>1,2</sup> | Ismaila Dabo<sup>1</sup> | Christina M. Rost<sup>3</sup>  | Jon-Paul Maria<sup>1</sup> 

<sup>1</sup>Department of Materials Science and Engineering, The Pennsylvania State University, University Park, Pennsylvania, USA

<sup>2</sup>Department of Physics, The Pennsylvania State University, University Park, Pennsylvania, USA

<sup>3</sup>Department of Physics and Astronomy, James Madison University, Harrisonburg, Virginia, USA

## Correspondence

Jon-Paul Maria, Department of Materials Science and Engineering, The Pennsylvania State University, University Park, PA 16802, USA.

Email: [jpm133@psu.edu](mailto:jpm133@psu.edu)

## Funding information

NSF, Grant/Award Numbers: DMR-1610844, DMR-1839087, DMR-2011839

## Abstract

High-entropy materials defy historical materials design paradigms by leveraging chemical disorder to kinetically stabilize novel crystalline solid solutions comprised of many end-members. Formulation diversity results in local crystal structures that are seldom found in conventional materials and can strongly influence macroscopic physical properties. Thermodynamically prescribed chemical flexibility provides a means to tune such properties. Additionally, kinetic metastability results in many possible atomic arrangements, including both solid-solution configurations and heterogeneous phase assemblies, depending on synthesis conditions. Local disorder induced by metastability, and extensive cation solubilities allowed by thermodynamics combine to give many high-entropy oxide systems utility as electrochemical, magnetic, thermal, dielectric, and optical materials. Though high-entropy materials research is maturing rapidly, much remains to be understood and many compositions still await discovery, exploration, and implementation.

## KEYWORDS

entropy, functional properties, high-entropy oxides, synthesis

## 1 | INTRODUCTION

### 1.1 | Introduction and scope

The entropy engineering paradigm opens new doors to a vast realm of novel materials with broad-ranging potential. High-entropy solid solutions emerged as a field of materials research following two reports in 2004 on concentrated multicomponent alloys.<sup>1,2</sup> Such alloys became

known as “high-entropy alloys” (HEAs), due to the large configurational entropy (i.e., quantity of possible atomic arrangements) of the solid-solution phase(s). Eleven years later, the concept was formally extended to oxide ceramics, initially termed “entropy-stabilized oxides” (ESOs).<sup>3</sup> These works defied historical materials design principles predicated on enthalpy and internal energy minimization by demonstrating that configurational entropy can stabilize novel solid solutions.

This is an open access article under the terms of the [Creative Commons Attribution](https://creativecommons.org/licenses/by/4.0/) License, which permits use, distribution and reproduction in any medium, provided the original work is properly cited.

© 2023 The Authors. *Journal of the American Ceramic Society* published by Wiley Periodicals LLC on behalf of American Ceramic Society.

The present review focuses on high-entropy oxides (HEOs), a subset of high-entropy ceramics (HECs) (including carbides, nitrides, borides, fluorides, etc.). A number of HEA,<sup>4</sup> HEO,<sup>5,6</sup> and HEC<sup>7–9</sup> reviews exist, including focused reviews on energy storage,<sup>10</sup> catalysis,<sup>11,12</sup> and magnetic properties.<sup>13</sup> General discussions and considerations for tailoring disorder in crystalline systems can be found in Ref. 14. A point of emphasis in the present review is how HEO behaviors often relate to metastability and nonequilibrium kinetics, despite the widespread usage of equilibrium thermodynamic models. Included are introductory sections describing notation and terminology; an early history of concerted HEO research; discussions of thermodynamics, kinetics, and defects of complex oxide solid solutions; computational considerations; discussions of HEO synthesis techniques in the context of kinetics and configuration space; and a brief overview of HEO functional properties.

To facilitate generality, we primarily consider a few relatively well-studied prototype HEO systems, namely, HEOs based on the rocksalt  $\text{Mg}_{1/5}\text{Co}_{1/5}\text{Ni}_{1/5}\text{Cu}_{1/5}\text{Zn}_{1/5}\text{O}$ ,<sup>3</sup> the oxygen-deficient fluorite derivative  $\text{Y}_{1/5}\text{La}_{1/5}\text{Ce}_{1/5}\text{Pr}_{1/5}\text{Sm}_{1/5}\text{O}_{2-\delta}$ ,<sup>15,16</sup> and spinel HEOs based on the CrMnFeCoNi “Cantor alloy.”<sup>1,17</sup> Interested readers can find more exhaustive tables of reported HEO<sup>5,9</sup> (or HEC<sup>7,9</sup>) compositions in prior reviews. Some remarks on notation: we employ fractional subscripts that reflect the nominal stoichiometry of the solution or HEO family. For example,  $\text{Mg}_{1/5}\text{Co}_{1/5}\text{Ni}_{1/5}\text{Cu}_{1/5}\text{Zn}_{1/5}\text{O}$  or  $(\text{Mg}_{1/5}\text{Co}_{1/5}\text{Ni}_{1/5}\text{Cu}_{1/5}\text{Zn}_{1/5})\text{O}$ , rather than shorthand notations such as  $\text{MgCoNiCuZnO}$  or  $(\text{Mg,Co,Ni,Cu,Zn})\text{O}$ . We also typically arrange the cations in order of increasing atomic number, except when clarity can be improved by doing otherwise: for example, writing  $\text{Sc}_{1/6}\text{Mg}_{1/6}\text{Co}_{1/6}\text{Ni}_{1/6}\text{Cu}_{1/6}\text{Zn}_{1/6}\text{O}$  to emphasize Sc addition to  $\text{Mg}_{1/5}\text{Co}_{1/5}\text{Ni}_{1/5}\text{Cu}_{1/5}\text{Zn}_{1/5}\text{O}$ .

## 1.2 | Taxonomy and classification of high-entropy oxides

Rost et al. initially employed “ESOs” to describe the material class represented by the prototype  $\text{Mg}_{1/5}\text{Co}_{1/5}\text{Ni}_{1/5}\text{Cu}_{1/5}\text{Zn}_{1/5}\text{O}$ <sup>3</sup>; however, many prefer the more general term “HEO.” We note that “entropy-stabilized,” discussed in Section 6.1, and “high-entropy” are in general not synonymous or interchangeable.<sup>18</sup>

Presently, we use the moniker HEO and qualitatively consider HEOs as the spectrum of crystalline oxide solid solutions loosely centered around four- or five-component equimolar cation collections populating one or more lattice sites with a correspondingly large maximum ideal

configurational entropy of mixing, which in many cases are kinetically (and practically) trapped in the metastable high-entropy solid-solution condition, which these diverse chemical formulations seem to prefer. More precise definitions of “high entropy” vary by author; some quantitative definitions for HEO and HEC systems are based on ideal maximum configurational entropy, derived entropy metrics<sup>19</sup> or relative elemental concentrations and number of sublattices.<sup>20</sup> To maintain brevity, generality, and inclusivity, we do not attempt to stratify HEO systems in this way.

## 2 | ENTROPY VERSUS DISORDER

The words “entropy” and “disorder” appear often in high-entropy materials literature, so their use in the present document warrants clarification upfront. As discussed by Styer,<sup>21</sup> the common analogy that entropy corresponds to disorder can be misleading, since it “invites us to think about a single configuration rather than a class of configurations.” Entropy itself is a quantity of statistical mechanics, as discussed in Section 6. When we describe HEOs as disordered, we are referring to the inherent local asymmetries within an HEO crystal, discussed in Section 3. The large entropy gain upon chemical mixing drives HEO phase formation, whereas the inherent disorder of HEO configurations gives rise to their emergent properties and functionality.

## 3 | DEFINING ATTRIBUTES OF SINGLE-PHASE HEOs

### 3.1 | Compositional flexibility

HEO crystals are solid solutions, not stoichiometric compounds; consequently, they possess extensive compositional flexibility. In addition, the high-entropy state fundamentally promotes solubility, and a high-entropy host can solubilize strongly misfit solutes more so than its low-entropy analogue.<sup>22</sup> Following this logic, since the intrinsic properties of a crystal depend upon the elements that comprise it, altering chemical composition provides an avenue for physical property tuning. In the  $\text{Mg}_{1/5}\text{Co}_{1/5}\text{Ni}_{1/5}\text{Cu}_{1/5}\text{Zn}_{1/5}\text{O}$  system, a single-phase structure can be maintained when deviating from equimolarity at the expense of an increased stability temperature.<sup>3</sup> In terms of properties, cation selection and concentration control can be leveraged to alter optical absorption features,<sup>23</sup> tune thermal conductivity,<sup>24</sup> or shift magnetic ordering temperatures.<sup>25–27</sup> Incorporating functional elements such as Li or Pt into  $\text{Mg}_{1/5}\text{Co}_{1/5}\text{Ni}_{1/5}\text{Cu}_{1/5}\text{Zn}_{1/5}\text{O}$

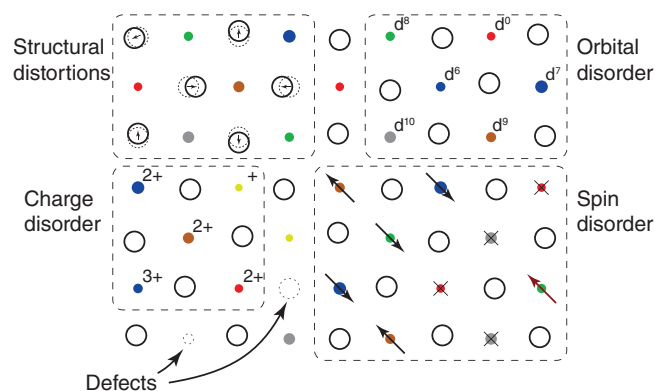


**FIGURE 1** Two-dimensional illustration of local asymmetry and disorder in an high-entropy oxide (HEO) crystal: local structural distortions (top-left); electron orbital disorder (top-right); ionic charge disorder and defects (bottom-left); magnetic spin disorder (bottom-right). Arrows in the bottom-right panel denote electron spin orientation.

results in electrochemical utility<sup>28</sup> or useful catalytic behavior,<sup>29</sup> respectively.

### 3.2 | Macroscopic symmetry and local asymmetry

Crystallinity is defined by the combination of local point symmetry and long-range translational symmetry. Relatively simple and high-symmetry parent structures that participate in high-entropy systems include rocksalt (general formula AO; space group symmetry  $Fm\bar{3}m$ ),<sup>3,25</sup> fluorite ( $AO_{2-\delta}$ ;  $Fm\bar{3}m$ ),<sup>15,30</sup> bixbyite (or C-type rare-earth oxide structure;  $A_2O_3$ ;  $Ia\bar{3}$ ),<sup>15,16</sup> perovskite ( $ABO_3$ ;  $Fm\bar{3}m$ ,  $Pbnm$ , or  $R\bar{3}c$ ),<sup>31–34</sup> spinel ( $AB_2O_4$  or  $A_3O_4$ ; typically  $Fd\bar{3}m$  or  $F\bar{4}3m$ ),<sup>17,26,35,36</sup> and pyrochlore ( $A_2B_2O_7$ ; typically  $Fd\bar{3}m$  or  $F\bar{4}3m$ ).<sup>37,38</sup> Fundamental studies on phase stability, cation site occupancy, and properties employing these simple structures continue to guide research and development of HEOs with other, more complex structures, including Ruddlesden–Popper phases,<sup>39</sup> silicate phases,<sup>40–42</sup> aluminates,<sup>43</sup> phosphates,<sup>44</sup> and magnetoplumbite structures.<sup>45</sup>

Although HEOs exhibit macroscopically averaged crystalline symmetry and compositional uniformity reminiscent of their conventional lower entropy counterparts,<sup>46</sup> they possess inherent local disorder and asymmetry, an attribute that can lead to functionality not found in more well-ordered, lower-entropy systems.<sup>14</sup> The simultaneous occurrence of structural distortions, charge disorder, orbital disorder, and magnetic disorder is illustrated schematically in Figure 1, as inspired by Meisenheimer and Heron.<sup>47</sup>

This local structural asymmetry is exemplified by Jahn–Teller distortions of  $CuO_6$  octahedra in quenched  $Mg_{1/5}Co_{1/5}Ni_{1/5}Cu_{1/5}Zn_{1/5}O$ .<sup>48–50</sup> The macroscopically averaged symmetry is cubic, but Jahn–Teller distortions necessitate local tetragonal symmetry. Cubic symmetry is globally sustained by the diversity of the constituents' ionic radii that produce “compensating” bond length and bond angle distributions. Experiment and theory suggest cations predominantly occupy their symmetry-prescribed lattice positions, whereas anions exhibit local displacements to accommodate them.<sup>48,51</sup>

Extreme chemical disorder results in complex local interactions and asymmetric fluctuations of structural and electromagnetic order parameters, giving rise to unique and sometimes unpredictable property dispersions, which lie outside interpolative predictions of end-member-averaged contributions.<sup>52</sup> For example, magnetic frustration can result in unusual magnetic phase structures,<sup>13</sup> and local restoring force disorder can produce remarkably low thermal conductivities compared to typical crystalline systems.<sup>24</sup> Manipulating this disorder may then provide another avenue for property tuning. However, this local disorder is also difficult to characterize, as discussed in Section 4.

## 4 | HEO CHARACTERIZATION

HEO physical properties can be measured in much the same way as other crystals, but correlating properties to local structure requires complementary multi-scale and multimodal analysis. Diffraction can probe the macroscopic crystal symmetry but fails to elucidate local structural nuances. Transmission electron microscopy provides high spatial resolution in two dimensions, but resolution in the third dimension requires extremely specialized approaches like ptychography.<sup>53–55</sup> Atom probe tomography can provide near-atomic resolution three-dimensional elemental mapping<sup>46</sup> but does not provide electronic, magnetic, or vibrational information. Spectroscopy can provide electronic and vibrational information with high-energy resolution but limited spatial resolution. X-ray absorption spectroscopy is particularly useful for characterizing HEOs, because it excites core electrons, providing element-specific electronic<sup>36,56–58</sup> and localized structural information.<sup>24,39,48</sup> Theoretical simulation helps fill the gaps by providing detailed structural and electronic information.<sup>51</sup> However, even modern computing clusters cannot yet practically consider every possible atomic configuration, so theory/model-informed configuration selection is crucial for accurately simulating an experimental sample set.

## 5 | HISTORICAL PERSPECTIVE

### 5.1 | High-entropy alloy development

In 1788, Franz Karl Achard published his book “Recherches sur les propriétés des alliages métalliques,” which presents observations of over 900 metallic alloy compositions, including many 4–7 component alloys mixed in equal weight proportions. Contrary to expectation and prediction, his experimental results illustrated that alloy properties often differ from their constituents.<sup>59</sup> Although he could be the first researcher to synthesize quinary to septenary multicomponent alloys, his work went unrecognized for centuries.<sup>60</sup>

The first widely recognized reports on equimolar, multi-component alloy solutions appeared in 2004 from Cantor et al.<sup>1</sup> and Yeh et al.<sup>2</sup> These reports introduced the terms “multi-principal element alloy” and HEA. The novel high-entropy alloying strategy unlocked vast realms of previously unexplored composition space, still not fully explored or understood. Much HEA research has emphasized single-phase solid solutions, but compositions often deliberately deviate from equimolarity and/or single-phase microstructures.<sup>61</sup> In terms of standout applications, many consider HEA systems future refractory structural materials, due to their mechanical robustness, high-temperature stabilities, and potential nano-phase domain structures.<sup>62</sup> For further reading, see a couple excellent HEA reviews.<sup>4,63</sup>

Prior to 2015, HEA researchers experimented with oxidizing atmospheres during thin film growth. Chen et al. reported one of the earliest HEO solutions: reactively sputtered  $\text{Al}_x\text{CrFeCoNiCu}$ -oxide films that exhibited spinel diffraction patterns.<sup>64</sup> These reports were harbingers to the more targeted HEO work discussed next.

### 5.2 | 2015: entropy-stabilized oxides

Rost et al. produced a particularly influential report in 2015 that explored the prototype composition  $\text{Mg}_{1/5}\text{Co}_{1/5}\text{Ni}_{1/5}\text{Cu}_{1/5}\text{Zn}_{1/5}\text{O}$ .<sup>3</sup> Constituents were chosen deliberately to test the hypothesis that configurational entropy can outweigh enthalpy and stabilize a five-component, equimolar oxide. The constituents vary in preferred bonding coordination, electronic orbital configuration, and electronegativity; and there exist pairs of constituents that do not exhibit extensive solubility (e.g., CuO and NiO). Intuitively, one may not expect this mixture to form a solid solution, but above  $\sim 875^\circ\text{C}$  the system stabilizes in a rocksalt solid solution at the cost of a positive mixing enthalpy,  $\sim 12 \text{ kJ mol}^{-1}$ . The

transition from multiphase to single-phase is reversible and endothermic, illustrated in Figure 2. Additionally, the solid-solution phase is chemically homogeneous: cations appear randomly distributed. These aspects of the  $\text{Mg}_{1/5}\text{Co}_{1/5}\text{Ni}_{1/5}\text{Cu}_{1/5}\text{Zn}_{1/5}\text{O}$  composition fit the definition for an entropy-stabilized phase, hence the original choice of acronym: ESO.<sup>3</sup> This report caught the attention of the ceramics community and set HEO and HEC research into motion.

### 5.3 | 2016–2017: early reports

2016 saw three important HEO reports. Bérardan et al. observed Li ionic conductivity in  $\text{Mg}_{1/5}\text{Co}_{1/5}\text{Ni}_{1/5}\text{Cu}_{1/5}\text{Zn}_{1/5}\text{O}$ -derived ceramics,<sup>65</sup> prompting future investigations for Li-ion storage applications. The same group measured high dielectric constants for a similar collection of HEOs.<sup>66</sup> Rak et al.’s density functional theory (DFT) calculations suggested a degree of charge transferability amongst cations in  $\text{Mg}_{1/5}\text{Co}_{1/5}\text{Ni}_{1/5}\text{Cu}_{1/5}\text{Zn}_{1/5}\text{O}$  with Li and Sc additions.<sup>51</sup>

Rost et al. studied the local structure of  $\text{Mg}_{1/5}\text{Co}_{1/5}\text{Ni}_{1/5}\text{Cu}_{1/5}\text{Zn}_{1/5}\text{O}$  in more depth with X-ray absorption fine structure, concluding that structural distortions primarily occur on the anion sublattice.<sup>48</sup> Meisenheimer et al. reported the first magnetic data for  $\text{Mg}_{1/5}\text{Co}_{1/5}\text{Ni}_{1/5}\text{Cu}_{1/5}\text{Zn}_{1/5}\text{O}$  in the form of magnetic exchange thin film heterostructures.<sup>67</sup> Berardan et al. reported electron paramagnetic resonance experiments, confirming the presence of Jahn–Teller distortions in  $\text{Mg}_{1/5}\text{Co}_{1/5}\text{Ni}_{1/5}\text{Cu}_{1/5}\text{Zn}_{1/5}\text{O}$ .<sup>50</sup> Djenadic et al.<sup>15</sup> and Sarkar et al.<sup>23</sup> reported a series of rare-earth-based HEO powders with fluorite or bixbyite structures, depending on synthesis conditions; the flagship composition being  $\text{Y}_{1/5}\text{La}_{1/5}\text{Ce}_{1/5}\text{Pr}_{1/5}\text{Sm}_{1/5}\text{O}_{2-\delta}$ . Jiang et al. reported first on bulk perovskite-structured HEOs.<sup>31</sup>

### 5.4 | 2018: rapid expansion, influential discoveries

2018 brought about further characterization of  $\text{Mg}_{1/5}\text{Co}_{1/5}\text{Ni}_{1/5}\text{Cu}_{1/5}\text{Zn}_{1/5}\text{O}$ , epitaxial crystal growth studies, more compositional discovery, thermal characterization of HEOs, and ground-breaking electrochemical studies. Anand et al. showed the utility of random and genetic algorithm sampling combined with molecular dynamics (MD) for analyzing the configurational energy landscape of  $\text{Mg}_{1/5}\text{Co}_{1/5}\text{Ni}_{1/5}\text{Cu}_{1/5}\text{Zn}_{1/5}\text{O}$ .<sup>68</sup> DFT simulations by Rak et al. suggested potential Jahn–Teller compressions as well as elongations in  $\text{Mg}_{1/5}\text{Co}_{1/5}\text{Ni}_{1/5}\text{Cu}_{1/5}\text{Zn}_{1/5}\text{O}$ .<sup>49</sup> Reports on epitaxial HEO





Interest in perovskite HEOs escalated. HEO perovskites showed indications of relaxor ferroelectricity.<sup>84–87</sup> Son et al. evaluated the electrocaloric effect of  $\text{Pb}(\text{Hf}_{1/5}\text{Zr}_{1/5}\text{Ti}_{1/5}\text{Nb}_{1/5}\text{Mn}_{1/5})\text{O}_3$  and  $\text{Pb}(\text{Hf}_{1/5}\text{Zr}_{1/5}\text{Ti}_{1/5}\text{Nb}_{1/5}\text{Al}_{1/5})\text{O}_3$ .<sup>88</sup> Patel et al. grew epitaxial  $(\text{La}_{1/5}\text{Pr}_{1/5}\text{Nd}_{1/5}\text{Sm}_{1/5}\text{Eu}_{1/5})\text{NiO}_3$  films exhibiting a metal–insulator transition.<sup>34</sup>

HEO thermodynamics also received needed attention. McCormack and Navrotsky elegantly reviewed solution thermodynamics in the context of HEOs, providing illustrative examples.<sup>18</sup> Ushakov et al. investigated high-temperature polymorphic phase transformations in lanthanide HEOs  $(\text{La}_{1/5}\text{Sm}_{1/5}\text{Dy}_{1/5}\text{Er}_{1/5}\text{X})_2\text{O}_3$  ( $\text{X} = \text{Nd, Gd, or Y}$ ).<sup>89</sup>

Further investigation of thermal conduction trends<sup>38,90</sup> led to interest in protective coatings<sup>91,92</sup> and thermoelectrics.<sup>93,94</sup>

Notable synthesis advancements include successful bulk crystal growth<sup>95,96</sup> (prior crystal growth was limited to epitaxial thin films) and investigation of nonequilibrium laser-induced annealing or crystallization techniques to produce nanostructured HEO particles potentially useful as catalysts.<sup>74,97,98</sup> Stenzel et al. reported the first triclinic HEO  $(\text{Mg}_{1/5}\text{Fe}_{1/5}\text{Ni}_{1/5}\text{Cu}_{1/5}\text{Zn}_{1/5})\text{MoO}_4$ ,<sup>99</sup> suggesting that structural and electrostatic compliance, not necessarily long-range symmetry, play a strong role in facilitating the high-entropy condition.

## 6 | SCIENTIFIC FOUNDATIONS

### 6.1 | Basic solution thermodynamics

Thermodynamic equilibrium occurs when the free energy of a system is minimized at a given set of thermochemical boundary conditions. Most often, temperature  $T$  and pressure  $P$  are chosen as experimental control variables. In this case, one considers the Gibbs free energy, often written:

$$G = U + PV - TS = H - TS \quad (1)$$

where  $T$  is temperature in Kelvin,  $S$  is entropy,  $H = U + PV$  is enthalpy,  $U$  is the internal energy,  $P$  is pressure, and  $V$  is volume. Considering the Gibbs free energy of phase formation  $\Delta G^f = \Delta H^f - T\Delta S^f$ , the “entropy-stabilized” condition implies that  $\Delta H^f > 0$  and there is a critical temperature above which  $T\Delta S^f$  drive phase formation. If  $\Delta H^f < 0$ , the phase is enthalpy-stabilized and forms at all temperatures.

In classical thermodynamics, entropy is related to the heat absorbed during an equilibrium reversible process in a closed system via  $\delta Q_{rev} = TdS$ , where  $\delta Q$  is an

infinitesimal quantity of heat. However, a discussion regarding configurational entropy benefits most from the statistical entropy relation first developed by Boltzmann, later rewritten by Max Planck:  $S = k_B \ln \Omega$ , where  $k_B$  is Boltzmann’s constant and  $\Omega$  is the number of microstates that define a given macrostate. One can consider  $\Omega$  as the number of possible ways to arrange matter and allocate available energy among a system of particles. Although a microstate is the precise description of a system at an instant in time, a macrostate is a collection of accessible microstates that determine macroscopic thermodynamic behavior during some period of time. At finite temperature, atoms undergo thermal oscillations, electronic excitations, and magnetic moment reorientations; and ensembles of atoms can undergo chemical mixing or phase transformations. Thus, total entropy of a crystal is determined by the number of possible atomic arrangements and the spectrum of vibrational modes, electron configurations, magnetic moment orientations, and so on associated with each atomic arrangement.

A crystal’s configurational entropy is determined by the number of possible atomic arrangements and can be calculated analytically using combinatorial analysis, Stirling’s approximation, and the Boltzmann hypothesis.<sup>100</sup>  $S^{config}$  per formula unit for a crystal with multiple sublattices and randomly distributed species on each sublattice follows the equation:

$$S^{config} \approx -R \sum_j m_j \sum_i X_{ij} \ln X_{ij} \quad (2)$$

where  $R$  is the universal gas constant,  $m_j$  is the multiplicity of lattice sites on sublattice  $j$  per formula unit, and  $X_{ij}$  is the molar fraction of species  $i$  on sublattice  $j$  (e.g., for a rocksalt AO,  $m_A = m_O = 1$ ; but for fluorite,  $\text{AO}_2$ ,  $m_A = 1$  and  $m_O = 2$ ). The analytical value for configurational entropy depends on normalization (e.g., per mole of formula units, per mole of atoms, or per mole of cations). Equation (2) rises to a maximum at equimolar compositions and increases with the number of constituents, visualized in Figure 2C. A common benchmark value is that of an ideal five-component equimolar solid solution:  $S^{config} = -R \ln 1/5 = R \ln 5 = 1.609R$ .

For a mixing reaction, a single-phase solution will form only if  $T\Delta S^{mix} > \Delta H^{mix}$  and  $\Delta G^{mix}$  is more negative than  $\Delta G^f$  for all other possible phase assemblies, potentially including intermediate compounds.<sup>18,63</sup> Since  $\Delta S^{config}$  typically dominates  $\Delta S^{mix}$ , entropy engineering is predicated on maximizing  $S^{config}$  of the solution phase to boost  $T\Delta S^{mix}$ .

To understand constituent solubility limits, one can consider components’ chemical potential<sup>18</sup> (i.e., partial molar

Gibbs free energy):

$$\mu_i = (\partial G / \partial X_i) \quad (3)$$

where  $X_i$  is the molar fraction of component  $i$ . The activity  $a_i$  and the activity coefficient  $\gamma_i$  relate to molar fraction via  $a_i = \gamma_i X_i$ . Activity and chemical potential are related by the equation:

$$\mu_i - \mu_i^0 = \Delta\mu_i = RT \ln a_i = RT \ln X_i \gamma_i = RT \ln X_i + RT \ln \gamma_i \quad (4)$$

where  $\mu_i^0$  is the chemical potential of component  $i$  in its reference state. The condition for ideal behavior is  $\gamma_i = 1$ , making the partial molar ideal Gibbs free energy of mixing:  $\Delta G_i^{ideal} = RT \ln X_i = T \Delta S_i^{config}$ . The nonideal (“excess,” denoted “XS”) partial molar Gibbs free energy of mixing is  $\Delta G_i^{XS} = RT \ln \gamma_i$ . Since  $\Delta G_i^{ideal}$  can be computed analytically, measurements of activities and activity coefficients (or excess free energies) provide an experimental link to thermodynamics in terms of chemical composition and temperature.

For a nonideal solution,  $\Delta G_i^{XS}$  contributions come from a gamut of sources, such as enthalpy of mixing; changes in vibrational entropy; structural transformation energies; surface and interface energies; magnetic effects; electronic effects; defect effects; and possibly other sources.<sup>18</sup> In other words,  $\Delta G_i^{XS}$  includes the sum of all contributions other than the ideal configurational entropy of mixing. At chemical equilibrium, Equation (4) equals zero and the concentration of a given constituent in solution is determined by the excess chemical potential and temperature:

$$X_i = \exp \left( -\frac{\Delta G_i^{XS}}{RT} \right) \quad (5)$$

Excess free energy terms can be negative or positive, serving to stabilize or destabilize the solid-solution phase respectively. If a chosen constituent has a different crystal structure from the solution phase (e.g., CuO or ZnO dissolved in a rocksalt phase), one can expect a positive  $\Delta G_i^{XS}$  contribution corresponding to the structural change. For nanostructures, surface free energies may influence solubility limits or favor one polymorph over another.<sup>18</sup> In the  $Y_{1/5}La_{1/5}Ce_{1/5}Pr_{1/5}Sm_{1/5}O_{2-\delta}$  system, nanoparticles can exhibit a fluorite diffraction pattern,<sup>15,101</sup> whereas bulk specimens<sup>16</sup> exhibit a bixbyte pattern, suggesting possible surface energy contributions. HEO systems with multivalent cations may experience a thermodynamic dependence on oxygen chemical potential, illustrated by the tunable valence state of Pr in  $Y_{1/5}La_{1/5}Ce_{1/5}Pr_{1/5}Sm_{1/5}O_{2-\delta}$ .<sup>102</sup> With high vacancy concentrations, one may consider potential

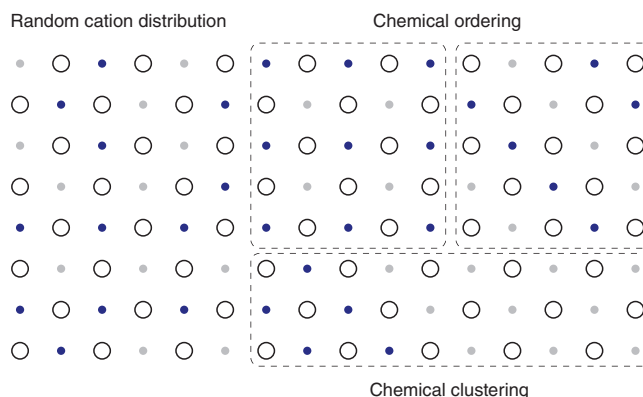


**FIGURE 3** Two-dimensional schematic comparing a random cation distribution (left); two different cation ordering schemes (top-right); and elemental clustering (bottom-right). Open circles represent oxygen atoms. Such configurations are allowed in a solid solution, though they are greatly outnumbered by random configurations. Tendencies for short- and long-range order depend on local interaction energies.

defect contributions to Equations (2) and (5). Epitaxial thin film growth may introduce nontrivial interface energies and mechanical contributions from epitaxial strain.<sup>103</sup> Though configurational entropy maximization provides the primary driving force for HEO solution formation, real systems experience nonideal thermodynamic forces that often act to destabilize solution phases at low temperatures.

## 6.2 | Chemical ordering

In ideal solutions,  $\Delta H^{mix} = 0$  and all configurations are equally probable. However, the probability of observing a segregated or orderly configuration is statistically low compared to apparently random or uniform configurations. Nonideal solution behavior ( $\Delta H^{mix} \neq 0$ ) can be indicative of energetically favorable short-range ordering (SRO), meaning certain atomic configurations possess a lower internal energy than others. Such tendencies bias the system's exploration of configuration space and can reduce configurational entropy below that of Equation (2) without breaking the bulk crystal symmetry. A two-dimensional example of SRO is illustrated in Figure 3, using a binary oxide solution for simplicity and clarity.

Salient examples of chemical ordering can be found in fluorite-derived oxide systems. Oxygen-deficient  $CeO_{2-\delta}$  and  $PrO_{2-\delta}$  are stable in a disordered fluorite structure at elevated temperature over a wide range of  $\delta$ . However, at lower temperatures  $TS$  is numerically too small to stabilize a disordered oxygen sublattice and oxygen vacancies undergo long-range ordering to form the

homologous series phases.<sup>104</sup> Bixbyite and pyrochlore structures can be regarded as oxygen-deficient fluorite-derived structures with fully ordered vacant oxygen sites and local lattice distortions. Solid solutions of such structures can readily exhibit SRO, despite single-phase diffraction patterns. For example,  $\text{Y}_2\text{O}_3\text{--CeO}_2$  solid solutions can exhibit nanometer-scale crystallographically coherent domains that correspond to local bixbyite-type ordering (reminiscent of  $\text{Y}_2\text{O}_3$ ) in a Ce-rich fluorite host lattice or vice versa.<sup>105</sup> Similar situations may arise in HEOs such as  $\text{Y}_{1/5}\text{La}_{1/5}\text{Ce}_{1/5}\text{Pr}_{1/5}\text{Sm}_{1/5}\text{O}_{2-\delta}$ , which can exhibit a single-phase fluorite-type or bixbyite-type diffraction patterns depending on synthesis conditions and thermal history.<sup>15,16,102</sup>  $\text{A}_6\text{B}_2\text{O}_{17}$  ( $\text{A} = \text{Zr}$  or  $\text{Hf}$ ;  $\text{B} = \text{Nb}$  or  $\text{Ta}$ ) commensurately modulated phases present another example where the structures exist through a competition of order and disorder; residual cation disorder in these phases with subsequent large configurational entropy is essential to stabilizing them at high temperatures.<sup>106</sup> SRO is common in oxides and the potential for spinodal transitions or stable intermediate phases further complicate the free energy landscape in oxide solutions.<sup>18</sup> Such situations should be considered when analyzing diffraction patterns of HEO systems.

### 6.3 | Broken ergodicity and configurational down-selection in HEOs

A common assumption in equilibrium statistical thermodynamic treatments is ergodicity: the equivalence of time and ensemble-averaged properties, implying a continuous exploration of accessible microstates during observation. In other words, an ergodic system is one at equilibrium; its properties are not changing in time and are uniform in space (i.e., no macroscopic property gradients). Realistically, physical systems possess broken ergodicity,<sup>107</sup> meaning certain collections of microstates are not explored on the timescales of a given observation. HEOs are often quenched to deliberately avoid phase decomposition or atomic reconfiguration, illustrated in Figure 4. When quenched, HEOs become non-ergodic, because configurational exploration depends on solid-state diffusion, a particularly slow process at ambient conditions. Additionally, HEOs exhibit a distribution of local migration energies that can give rise to indirect long-range diffusion pathways, potentially hindering rapid and complete configurational exploration. Typical observation at room temperature may effectively sample the vibrational, electronic, and magnetic microstates, but only one or a small number of atomic configurations. As such, Equation (2) does not necessarily correspond to the configurational entropy of a quenched HEO specimen during observation, rather it corresponds

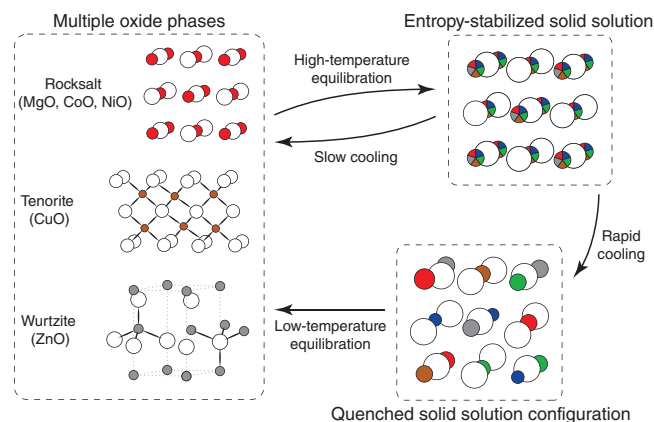


**FIGURE 4** Flowchart illustrating phase progression in the  $\text{Mg}_{1/5}\text{Co}_{1/5}\text{Ni}_{1/5}\text{Cu}_{1/5}\text{Zn}_{1/5}\text{O}$  system. At temperatures below  $\sim 875^\circ\text{C}$ , the equilibrium state is a mixture of oxide phases (left). Heating above  $\sim 875^\circ\text{C}$  stabilizes an equimolar rocksalt solid solution, consisting of all possible atomic configurations (top-right). Rapid cooling from high temperature kinetically freezes one (or a few) solution configuration(s) (bottom-right). Slow-cooling from high-temperature equilibrium or reannealing at intermediate or low temperature results in phase separation as the system is kinetically allowed to approach equilibrium.

to the ideal configurational entropy under equilibrium ergodic conditions.

On the pathway from high temperature or high kinetic energy (i.e., high effective temperature) synthesis conditions to room temperature, many-cation solid solutions like  $\text{Mg}_{1/5}\text{Co}_{1/5}\text{Ni}_{1/5}\text{Cu}_{1/5}\text{Zn}_{1/5}\text{O}$  will energetically prefer a transition from the limiting case of a random solid solution to one that exhibits chemical order. This transition can be slow, while cooling rates can be fast, which enables one to experimentally access a spectrum of states with variable ordering expressions, and to freeze them into persistent and probe-able metastable configurations. These configurations then represent nonequilibrium states characterized by a variable degree of entropic spending, where one sacrifices configurations for structural order.

Depending on the synthesis and analysis history of a particular HEO sample and its' excess entropy options, it may "spend" some of its configurational entropy and limit the number of explored configurations to those with relatively low energy. In other words, tendencies for chemical ordering can result in quenched configurations that do not represent what we expect of a random solid solution. For example, consider quenching an  $\text{Mg}_{1/5}\text{Co}_{1/5}\text{Ni}_{1/5}\text{Cu}_{1/5}\text{Zn}_{1/5}\text{O}$  sample for study. Above  $\sim 875^\circ\text{C}$ , a rocksalt solid solution phase is thermodynamically stable and comprised of all possible cation configurations. Simulations suggest a correlation between configurational energy and the number of Cu–Cu pair interactions.<sup>68</sup> During cooling, as  $TS$  decreases, atoms



might rearrange into a subset of rocksalt configurations with more Cu–Cu pair interactions to reduce total energy, resulting in a quenched single phase with a nonrandom Cu occupancy or local distortion. In the limit of slow cooling, energy-reducing atomic rearrangement results in CuO precipitation from the rocksalt phase.<sup>75,108</sup> Configurational down-selection was observed in quenched  $\text{Ti}_{1/5}\text{Zr}_{1/5}\text{Sn}_{1/5}\text{Ce}_{1/5}\text{Hf}_{1/5}\text{O}_2$  ceramics, which exhibited a single-phase diffraction pattern, but clear Ce clustering near grain boundaries.<sup>71</sup> In principle, time and temperature are not the only variables that can affect observed atomic configurations and phase assemblies; other boundary conditions, such as applied fields, stress, or oxygen chemical potential, may influence the free energy landscape and bias configurational exploration during synthesis and recovery.

## 6.4 | Defects and charge neutrality in HEOs

As with all real crystals, HEOs exhibit defects. However, HEOs are by their nature disordered and one might argue they are entirely defective. Here, we primarily consider point defects that occur either through changes in oxygen stoichiometry or aliovalent cation substitution (aliovalent relative to the idealized parent crystal structure). At this early moment in HEO research, special attention is paid to charge compensation, a necessary condition in ionic crystals. Early HEO works suggest that HEO lattices can host a wide range of defect concentrations, which serve to inflate the already large configurational entropy, provided they are randomly distributed. In terms of physical properties, doping and light chemical substitutions can affect elastic properties,<sup>109</sup> alter magnetic response,<sup>110</sup> drastically improve catalytic performance,<sup>29,73</sup> or induce luminescence<sup>111</sup> in HEO crystals.

### 6.4.1 | Intrinsic defects

In addition to uncharged intrinsic defects mediated by temperature (e.g., Schottky or Frenkel defects, HEO defect chemistry can depend on both  $T$  and oxygen chemical potential (or oxygen partial pressure  $p_{\text{O}_2}$ ), potentially leading to charged defects.<sup>112</sup> In the prototype  $\text{Mg}_{1/5}\text{Co}_{1/5}\text{Ni}_{1/5}\text{Cu}_{1/5}\text{Zn}_{1/5}\text{O}$  system, X-ray photoelectron spectroscopy<sup>66,113,114</sup> and X-ray absorption spectroscopy<sup>79</sup> suggest all 2+ cations in well-prepared specimens. However, defect studies as a function of  $p_{\text{O}_2}$  suggest potential oxygen vacancy concentrations as high as 7% without observable phase decomposition; a larger concentration than is typical for the end-member oxides.<sup>77</sup> Simulated

stress analyses suggest Cu reduction can compensate for local stresses arising from Jahn–Teller distorted octahedra.<sup>108</sup> Characterization of oxygen vacancies in  $(\text{Cr}_{1/5}\text{Mn}_{1/5}\text{Fe}_{1/5}\text{Co}_{1/5}\text{Ni}_{1/5})_3\text{O}_4$ <sup>78</sup>; variable Pr valence and oxygen stoichiometry in  $\text{Y}_{1/5}\text{La}_{1/5}\text{Ce}_{1/5}\text{Pr}_{1/5}\text{Sm}_{1/5}\text{O}_{2-\delta}$ <sup>102</sup>; oxygen vacancies in  $(\text{Mn}_{1/5}\text{Fe}_{1/5}\text{Co}_{1/5}\text{Ni}_{1/5}\text{Zn}_{1/5})\text{Fe}_2\text{O}_4$ <sup>115</sup>; and  $\text{Co}^{3+}$  in  $\text{Mg}_{1/5}\text{Co}_{1/5}\text{Ni}_{1/5}\text{Cu}_{1/5}\text{Zn}_{1/5}\text{O}$  films<sup>116</sup> illustrate a tolerance for intrinsic point defects in HEO systems with at least one multivalent cation. The chemical sophistication and configurational degrees of freedom in HEO systems may facilitate a variety of complex defect structures and defect interactions not yet characterized.

### 6.4.2 | Extrinsic defects and charge transferability

HEO crystals can tolerate large concentrations of aliovalent cations, such as  $\text{Li}^+$  in rocksalt HEOs<sup>65,66,76</sup> or 3+ cations in fluorite HEOs.<sup>15,30,111,117</sup> The concentration of necessary charge-compensating defects depends on the substituent concentration and is subject to Equation (5). Combined X-ray photoelectron spectroscopy and weight loss analysis suggests that in Li-modified  $\text{Mg}_{1/5}\text{Co}_{1/5}\text{Ni}_{1/5}\text{Cu}_{1/5}\text{Zn}_{1/5}\text{O}$ ,  $\text{Co}^{3+}$  is produced as charge compensation for Li concentrations up to ~16%, whereas oxygen vacancies are generated upon further Li incorporation.<sup>76</sup> Such charge transferability is supported by DFT simulations.<sup>51</sup> Cation valence shifts indicative of charge transfer have also been observed in Na-modified  $\text{Mg}_{1/5}\text{Co}_{1/5}\text{Ni}_{1/5}\text{Cu}_{1/5}\text{Zn}_{1/5}\text{O}$ .<sup>118</sup> Fluorite-structured HEOs with significant 3+ cation concentrations likely possess high oxygen vacancy concentrations, though local chemical ordering into oxygen-deficient fluorite derivative structures is always a possibility. Aliovalent ion inclusion is not limited to the cation sublattice, illustrated by F-containing rocksalts.<sup>58</sup>

### 6.4.3 | Aliovalent co-substitution

A significant observation is the potential coexistence of aliovalent cations in proportions that provide net charge neutrality without charged defects. An early example is equal co-incorporation of  $\text{Li}^+$  and  $\text{Ga}^{3+}$  in otherwise divalent rocksalt HEOs.<sup>65,66</sup> Other salient examples include the perovskites  $(\text{Na}_{1/5}\text{Bi}_{1/5}\text{Ca}_{1/5}\text{Sr}_{1/5}\text{Ba}_{1/5})\text{TiO}_3$ ,<sup>84</sup> with formal valence states of 1+, 2+, and 3+ on the *A*-site, and  $\text{Ba}(\text{Yb}_{1/5}\text{Y}_{1/5}\text{Zr}_{1/5}\text{Yb}_{1/5}\text{W}_{1/5})\text{O}_3$ , with formal valences of 3+, 4+, and 6+ on the *B*-site.<sup>119</sup> Valence combinations that provide net charge neutrality and obviate charge-balancing point defect formation can expand the compositional space

available to HEO systems beyond just isovalent cation collections. However, with collections of aliovalent cations on a common sublattice, one might consider the potential for nonrandom ordering or clustering that localizes charge neutrality.

## 7 | COMPUTATIONAL CONSIDERATIONS

HEO computational analysis complements experiments in at least two significant ways. First, simulations can reveal the state of the constituent atoms in their chemical environments to understand and predict the local mechanisms that control their collective electronic, optical, magnetic, and mechanical responses. Second, the thermodynamic stability and kinetic evolution of HEOs can be systematically examined for representative swaths of the configurational space. These capabilities give simulations predictive power to assist the design of HEO systems.

### 7.1 | Local analysis

Computational methods, such as DFT and MD, are privy to atomistic information that may not be directly accessible by microscopic and spectroscopic measurements, including atomic displacements, electronic hybridization, and magnetic and electric polarization. This information is critical to explain short-range interactions and long-range phenomena; electronic-structure simulations have helped understand charge transfer among cations,<sup>51</sup> lattice distortions,<sup>48,49,120,121</sup> and magnetic states<sup>80</sup> in HEOs. MD simulations have shown that cation ordering and phase stability in  $\text{Mg}_{1/5}\text{Co}_{1/5}\text{Ni}_{1/5}\text{Cu}_{1/5}\text{Zn}_{1/5}\text{O}$  are influenced by Cu–Cu pair interactions<sup>68</sup> and local mechanical stresses.<sup>68,108</sup> Additionally, DFT calculations demonstrated that local variations in cation–oxygen bond length relative to binary oxide constituents result in local distortions and strain that directly influence vacancy formation energies.<sup>122</sup>

### 7.2 | Predicting and analyzing phase stability

The ability to adopt multiple configurations is essential to the phase stability of high-entropy systems. Many descriptors and metrics (in addition to ideal configurational entropy) exist to classify HEOs and predict stable mixtures, including metrics related to atomic size distributions, computed formation enthalpies, and valence electron concentrations.<sup>123</sup> Since the ability to adopt mul-

tiple configurations is essential to the phase stability of high-entropy systems, a recently proposed descriptor of particular interest is the “entropy forming ability” (EFA) that is defined as the inverse standard deviation of the configurational energy distribution<sup>124</sup>; a narrow distribution of energies (corresponding to a high EFA) implies that less thermal energy is required for the system to explore the distribution of configurations and form a solid solution. For example, predictions for the local enthalpy distributions of  $\text{Mg}_{1/5}\text{Co}_{1/5}\text{Ni}_{1/5}\text{Cu}_{1/5}\text{Zn}_{1/5}\text{O}$  based on first-principles near-neighbor energies and cluster sampling suggest that this HEO has the narrowest configurational energy distribution among divalent rocksalt compositions,<sup>125</sup> which likely contributes to the reproducible occurrence of single-phase transitions during synthesis.

Additionally, there exist well-established thermodynamic models to predict solution behavior and phase diagrams for multicomponent systems. For instance, CALPHAD (calculated phase diagram) has been extensively exploited for HEA design<sup>4</sup> and has been shown to provide reliable phase diagrams for high-entropy systems provided that the database of free-energy parameters is accurate and complete.<sup>126</sup> The defect chemistry and mixing behavior of HEOs can also be modeled using CALPHAD<sup>112</sup> to illuminate the role of local defects on thermodynamic stability. CALPHAD may thus serve as a valuable tool for studying HEOs, particularly when the properties of interest (e.g., electron or ion transport properties) depend strongly on defects.<sup>112</sup>

### 7.3 | On configurational sampling

Balancing predictive accuracy and computational cost is one of the main challenges in simulating HEOs. Since an exhaustive exploration of the massive configurational space is practically intractable for these systems, the choice of sampling method is critical to the accuracy of computational predictions. Electronic-structure simulations of HEOs often consider a small number of special quasi-random structures<sup>37,49,51,80</sup> to reproduce the radial interatomic correlations of a perfectly random solution. These large simulation cells can capture midrange interactions (typically over several unit cells) but may fail to describe the nuances of local configuration variability in HEOs. Using supercells of reduced size, symmetrically inequivalent structures (SISs) can be sampled exhaustively using DFT.<sup>124</sup> Nevertheless, small simulation sizes and periodic boundary conditions limit the number of accessible configurations to account for clustering or ordering using the SIS approach. This limitation is problematic for complex compositions such as  $\text{Sc}_{1/6}\text{Mg}_{1/6}\text{Co}_{1/6}\text{Ni}_{1/6}\text{Cu}_{1/6}\text{Zn}_{1/6}\text{O}$ ,

$\text{Y}_{1/5}\text{La}_{1/5}\text{Ce}_{1/5}\text{Pr}_{1/5}\text{Sm}_{1/5}\text{O}_{2-\delta}$ , and  $(\text{Y}_{1/5}\text{La}_{1/5}\text{Nd}_{1/5}\text{Sm}_{1/5}\text{Gd}_{1/5})(\text{Cr}_{1/5}\text{Mn}_{1/5}\text{Fe}_{1/5}\text{Co}_{1/5}\text{Ni}_{1/5})\text{O}_3$ . Predicting long-range ordering in HEOs may require approaches that combine DFT with Monte Carlo or MD techniques,<sup>37</sup> or with cluster expansion methods.<sup>58</sup> Recent development of evolutionary algorithms, including the cuckoo search,<sup>127</sup> the hybrid cuckoo search,<sup>128</sup> and genetic algorithms,<sup>68</sup> may help automate computational analysis of high-entropy materials. Notably, machine-learning methods including deep learning<sup>129</sup> have been employed to obtain MD potentials from first-principles datasets for high-entropy carbides and may ultimately be of immense utility for modeling HEOs.

## 8 | HEO SYNTHESIS

Experimental HEO specimens can be synthesized using many different techniques and under a range of conditions,<sup>5,9,123</sup> provided the oxygen chemical potential is suitable for metal-oxide formation and the system is granted access to atomic configurations that correspond to a solid-solution macrostate. This can be accomplished thermodynamically or kinetically. Only in the case where a system is given sufficient energy and time to spontaneously explore all solid-solution configurations will thermodynamic stabilization occur. In many five-cation formulations, particularly those with diverse constituents, this condition is outside the condensed phase stability window. However, it is possible to give a many-component system thermal access to a solid solution configuration by traversing an intermediate, but very high effective temperature excited state, such as plasma. Solid solution configurations can be kinetically stabilized by nanosecond-length quenching from the  $10^4$  K vapor phase with no time for mass transport after condensation to spend configurational entropy. In this manner, metastable HEO crystals exhibit a configurational dependence on thermal history and kinetics, similar to glassy materials. As such, synthesis conditions can influence the recovered microstructure, atomic structure, and properties of experimental HEO specimens.

Common HEO synthesis techniques include solid-state reaction, solution precipitation, and physical vapor deposition (PVD). Each technique results in a different sample microstructure. Dense bulk ceramics can be sintered, nanopowders can be precipitated from solution, and crystals can be grown using vapor deposition. Each technique differs in terms of initial state, kinetics, and pathways through configuration space. Solid-state reaction employs a low-entropy initial state and relies upon solid-state diffusion for reactant intermixing. It also allows control over cooling rate; specimens can be quenched to retain

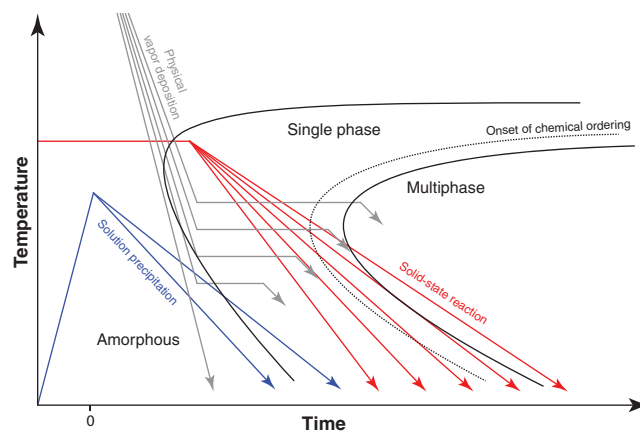


**FIGURE 5** Qualitative time–temperature–transformation diagram illustrating the different kinetics of common high-entropy oxide (HEO) synthesis methods. Red indicates solid-state reactive sintering, blue indicates solution combustion or powder precipitation techniques, and gray indicates high-energy physical vapor deposition techniques such as pulsed laser deposition (PLD) and sputtering. Note the variable cooling rates possible during reactive sintering. During vapor deposition, choice of growth temperature and growth time results in many possible pathways through the diagram.

a chemically homogeneous atomic distribution or cooled slowly to allow for energy-reducing atomic reconfiguration. In this case, the opportunities to explore metastability are most limited. Solution precipitation employs a high-entropy initial state—reactants dissolved in solution—and nonequilibrium kinetics. The high-entropy initial state provides shorter pathways through configuration space to random solid solution nucleation, allowing nonequilibrium HEO synthesis at relatively low temperatures compared to solid-state reaction. PVD also employs a high-entropy initial state and involves nonequilibrium condensation and crystallization onto a relatively cold substrate. The substrate temperature and net growth rate during PVD allow exquisite control of configurational exploration and relaxation during film growth. If a film is grown slowly, reconfiguration might result in nonrandom atomic configurations or even secondary phase precipitation. These differences are portrayed schematically in the form of a time–temperature–transformation (TTT) diagram (Figure 5). The TTT diagram includes a dashed line representing the onset of observable chemical ordering that may occur prior to macroscopic phase separation or secondary phase nucleation.

### 8.1 | Solid-state reaction

Many HEO experiments employ solid-state reactions to obtain dense bulk ceramic samples.<sup>3,17,31,48,65,66</sup> A standard

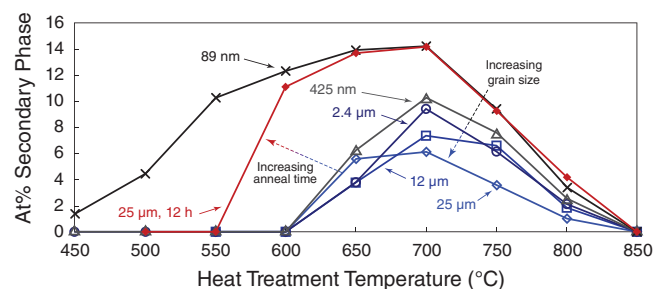


**FIGURE 6** Role of grain size on phase spectrum behavior in the  $\text{Mg}_{1/5}\text{Co}_{1/5}\text{Ni}_{1/5}\text{Cu}_{1/5}\text{Zn}_{1/5}\text{O}$  system: atomic percent (at%) secondary phase (tenorite) as a function of heat treatment temperature. All heat treatments were performed on single-phase specimens for 2 h, except the sample with an average grain size  $25\ \mu\text{m}$  that was treated for 12 h. As-consolidated average grain size values are labeled. Source: Figure adapted from Ref. 75 (CC BY 4.0).

tube-style furnace can approach equilibrium conditions in a controlled atmosphere if dwell times are long and temperature excursions are slow. Optionally introducing mechanical pressure (hot pressing, HP), electric fields (flash sintering, FS), or both (spark plasma sintering, SPS) can accelerate reaction times. HP,<sup>130</sup> FS,<sup>85,131–133</sup> and SPS<sup>30,75,91,134</sup> have been successfully applied to synthesize HEO ceramics. Notably, FS can rapidly react single-phase  $\text{Mg}_{1/5}\text{Co}_{1/5}\text{Ni}_{1/5}\text{Cu}_{1/5}\text{Zn}_{1/5}\text{O}$  with minimal applied external temperature<sup>132</sup> and SPS can create dense ceramics with small grain sizes.<sup>75</sup>

Assuming no liquid phase is introduced or generated, solid-state interdiffusion limits reaction rates. In the  $\text{Mg}_{1/5}\text{Co}_{1/5}\text{Ni}_{1/5}\text{Cu}_{1/5}\text{Zn}_{1/5}\text{O}$  system, upon increasing temperature, MgO, NiO, and CoO mix first into a three-component rocksalt phase. Zn then enters the rocksalt solid-solution, followed lastly by Cu.<sup>135</sup> Direct extraction from the furnace (air-quenching) appears sufficient to retain the solid-solution state,<sup>3</sup> but slow cooling rates or subsequent exposure to intermediate temperatures result in CuO precipitation.<sup>75,108</sup> The amount of CuO second phase depends on temperature, time, and grain size; illustrated in Figure 6.<sup>75</sup> Not all HEO systems exhibit rapid phase transformation kinetics. Bixbyite  $\text{Y}_{1/5}\text{La}_{1/5}\text{Ce}_{1/5}\text{Pr}_{1/5}\text{Sm}_{1/5}\text{O}_{2-\delta}$  and similar HEOs do not require aggressive quench rates<sup>16</sup> and other lanthanide HEOs appear to resist phase decomposition at intermediate temperatures.<sup>89,136</sup> Correspondingly, such systems require either small particle sizes or long reaction times to obtain a single phase in the first place.

Other solid-state synthesis methods of note include mechanical-induced (mechanochemical) synthesis of  $\text{Mg}_{1/5}\text{Co}_{1/5}\text{Ni}_{1/5}\text{Cu}_{1/5}\text{Zn}_{1/5}\text{O}$ <sup>137</sup> and a polymeric entrapment reactive sintering method employed to synthesize Ruddlesden–Popper structured bulk ceramics.<sup>138</sup> No doubt

other advanced ceramic synthesis methods or variations will show success for HEO synthesis.

## 8.2 | Solution precipitation

Various forms of solution-based precipitation processes have been employed to synthesize single-phase HEO powders or stoichiometric precursor powders, including coprecipitation,<sup>102,118,139</sup> solution combustion synthesis,<sup>108,140,141</sup> hydrothermal-assisted precipitation,<sup>142,143</sup> sol–gel synthesis,<sup>56,144–146</sup> ultrasonication-based synthesis,<sup>147</sup> and nebulized spray pyrolysis (NSP).<sup>15,32,148</sup> Soluble nitrate salts serve as excellent precursors for this purpose. If the desired phase structure is not obtained directly, the inherently short length scales and intraparticle stoichiometry facilitate subsequent calcination and/or densification.

An advantage of solution-based synthesis is homogeneous mixing of reactants in their initial state, directly contrasting solid-state reaction. If the solution is sufficiently homogeneous and reaction conditions are suitable, the most readily available kinetic pathway may be direct nucleation of the desired HEO phase, even if some amorphous material remains.<sup>140</sup> The presence of a single crystalline substrate may provide a kinetic pathway toward epitaxial crystal growth from solution, as illustrated by epitaxial nickelate films synthesized from acetate precursors via a sol–gel technique with control over crystal orientation.<sup>146</sup> The NSP process deserves some attention. High reactor temperatures (potentially exceeding  $1000^\circ\text{C}$ ) and rapid precipitation kinetics are well-suited for direct HEO nanopowder synthesis. NSP can synthesize nanocrystalline  $\text{Mg}_{1/5}\text{Co}_{1/5}\text{Ni}_{1/5}\text{Cu}_{1/5}\text{Zn}_{1/5}\text{O}$ , rare-earth-based HEOs such as  $\text{Y}_{1/5}\text{La}_{1/5}\text{Ce}_{1/5}\text{Pr}_{1/5}\text{Sm}_{1/5}\text{O}_{2-\delta}$ , and various  $\text{A}^{3+}\text{B}^{3+}\text{O}_3$  orthorhombic perovskites<sup>15,32,148</sup> in a single step.

## 8.3 | Physical vapor deposition

Of the various PVD techniques, PLD<sup>3,22,24,34,67,69,70,116,120,121,150–152</sup> and sputtering<sup>153,154</sup> are apt to synthesize HEOs. During condensation from the vapor or plasma phase, particles likely deposit randomly on the substrate, providing a short kinetic pathway to direct HEO nucleation. Work on  $\text{Sc}_{1/6}\text{Mg}_{1/6}\text{Co}_{1/6}\text{Ni}_{1/6}\text{Cu}_{1/6}\text{Zn}_{1/6}\text{O}$  suggests a large “effective temperature” during PLD that facilitates nucleation of highly metastable HEO phases.<sup>22</sup> The combination of nonequilibrium kinetics and direct nucleation pathways allow  $\text{Mg}_{1/5}\text{Co}_{1/5}\text{Ni}_{1/5}\text{Cu}_{1/5}\text{Zn}_{1/5}\text{O}$  growth at substrate temperatures as low as  $200^\circ\text{C}$ .<sup>70,116</sup>



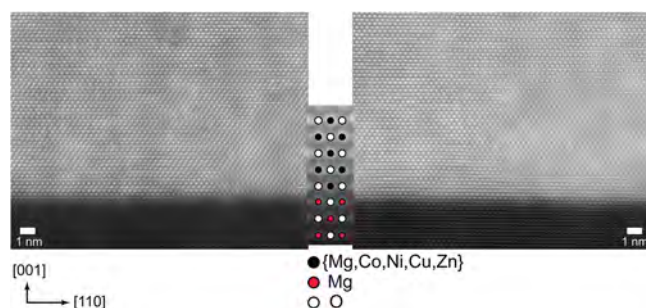


**FIGURE 7** HAADF-STEM images viewed along the  $[1\bar{1}0]$  zone axis of  $\text{Mg}_{1/5}\text{Co}_{1/5}\text{Ni}_{1/5}\text{Cu}_{1/5}\text{Zn}_{1/5}\text{O}$  grown on (100)-MgO by pulsed laser deposition (PLD) at substrate temperatures of 200°C (left) and 500°C (right). Center inset magnified from the right-hand image to show atomic positions. *Source:* Figure adapted with permission from Ref. 116; copyright 2020 American Physical Society.

Use of properly prepared single crystal substrates facilitates epitaxial film growth.<sup>3,22,24,34,39,67,69,70,116,120,121,150,151</sup> Atomic-resolution electron microscopy of epitaxial interfaces can be found in Figure 7 and Refs. 69, 116, 150. Despite the local disorder inherent to HEOs, epitaxial films can exhibit remarkable crystalline quality, providing an excellent platform for structural,<sup>116,121</sup> optical,<sup>116</sup> thermal,<sup>24,69</sup> mechanical,<sup>24</sup> electron transport,<sup>39</sup> and magnetic<sup>67,120,149,151</sup> characterization. The substrate can induce epitaxial stabilization,<sup>103</sup> illustrated by the synthesis of thin  $(\text{La}_{1/5}\text{Pr}_{1/5}\text{Nd}_{1/5}\text{Sm}_{1/5}\text{Eu}_{1/5})\text{NiO}_3$  films<sup>34</sup> and Ruddlesden-Popper phase  $(\text{La}_{1/5}\text{Pr}_{1/5}\text{Nd}_{1/5}\text{Sm}_{1/5}\text{Eu}_{1/5})_2\text{CuO}_4$ <sup>150</sup> films. Recent work also demonstrates an ability to tune properties via epitaxial strain.<sup>149,151</sup>

## 8.4 | Bulk single crystals, melt solidification, and laser heating

Recently, researchers began reporting HEO solidification from melts, including instances of bulk single crystal growth. Optical floating zone was employed to grow large pyrochlore-structured  $(\text{Gd}_{1/5}\text{Tb}_{1/5}\text{Dy}_{1/5}\text{Er}_{1/5}\text{Yb}_{1/5})_2\text{Ti}_2\text{O}_7$  crystals<sup>95</sup> and a micro-pulling-down method was used to obtain garnet-structured  $(\text{Y}_{1/6}\text{Gd}_{1/6}\text{Tb}_{1/6}\text{Dy}_{1/6}\text{Ho}_{1/6}\text{Lu}_{1/6})_3\text{Al}_5\text{O}_{12}$  crystals.<sup>96</sup> Bulk crystal growth from a melt typically requires congruent melting and resolidification, a condition potentially complicated by the presence of four or more constituents in significant amounts. Regardless, the successful growth of HEO bulk crystals presents opportunities for the future of HEO research and development.

In addition to crystal growth, rapid solidification from a melt can realize HEOs, due to nonequilibrium cooling

rates. Laser melting and splat quenching were employed for a series of high-entropy rare-earth sesquioxides as part of a study on the high-temperature phase transitions,<sup>89</sup> demonstrating utility for synthesizing refractory HEO solutions.

Strong kinetics-driven processes including laser scanning ablation and transient laser heating have been employed to synthesize HEO nanoparticles and to promote control of crystal phase formation.<sup>97,98,155</sup> Similar techniques employing nonequilibrium solidification may prove useful in future HEO work.

## 9 | FUNCTIONAL PROPERTIES

### 9.1 | Electrochemical utility

#### 9.1.1 | Energy storage

HEOs quickly garnered interest as electrode and electrolyte materials.<sup>10,156</sup> In particular,  $\text{Mg}_{1/5}\text{Co}_{1/5}\text{Ni}_{1/5}\text{Cu}_{1/5}\text{Zn}_{1/5}\text{O}$  and related rocksalt systems exhibit promising performance as anodes in Li ion electrochemical cells.<sup>28,113,114,157,158</sup>  $\text{Mg}_{1/5}\text{Co}_{1/5}\text{Ni}_{1/5}\text{Cu}_{1/5}\text{Zn}_{1/5}\text{O}$  itself outperforms both its four-component derivatives<sup>28</sup> and  $\text{Co}_3\text{O}_4$ .<sup>113</sup> Configurational entropy appears to facilitate large alkali ion solubility while inhibiting detrimental microstructural evolution during operation. Controllable particle morphologies provide an avenue for further improving electrode performance.<sup>114</sup> In situ characterization during lithiation indicates that multiple cations contribute to reduction and oxidation by changing valence.<sup>57,159</sup> Spinel HEOs have also shown promise as Li ion anodes,<sup>35,143,160,161</sup> notably including the prototype  $(\text{Cr}_{1/5}\text{Mn}_{1/5}\text{Fe}_{1/5}\text{Co}_{1/5}\text{Ni}_{1/5})_3\text{O}_4$ .<sup>143,161</sup> Investigated HEO cathode materials include rocksalts with Li and F in the starting composition,<sup>58,162</sup> and Li-<sup>163</sup> or Na-containing<sup>164</sup> layered structures. Systematic studies on rocksalt HEO cathodes reveal that, although increasing the number of constituents (increasing configurational entropy) helps inhibit detrimental SRO, intelligent cation selection is key to mitigating detrimental charge transfer mechanisms and optimizing performance.<sup>58</sup>

Potential HEO application in energy storage also extends to solid oxide fuel cells (SOFCs), owing to thermochemical stability and mixed ionic-electronic conductivity. Example compositions include  $\text{La}_{1-x}\text{Sr}_x(\text{Cr}_{1/5}\text{Mn}_{1/5}\text{Fe}_{1/5}\text{Co}_{1/5}\text{Ni}_{1/5})\text{O}_{3-\delta}$ ,<sup>165</sup>  $(\text{La}_{1/5}\text{Pr}_{1/5}\text{Nd}_{1/5}\text{Sm}_{1/5}\text{Sr}_{1/5})\text{MnO}_{3-\delta}$ ,<sup>166</sup> and  $\text{La}(\text{Mn}_{1/5}\text{Fe}_{1/5}\text{Co}_{1/5}\text{Ni}_{1/5}\text{Cu}_{1/5})\text{O}_{3-\delta}$ .<sup>167</sup> Such materials compete with conventional  $\text{La}_{1-x}\text{Sr}_x\text{MnO}_{3-\delta}$  electrodes and appear to resist large drifts in polarization resistances that arise from reconstruction and reactions

at the electrolyte interface.<sup>166,167</sup> Additionally,  $\text{Mg}_{1/5}\text{Co}_{1/5}\text{Ni}_{1/5}\text{Cu}_{1/5}\text{Zn}_{1/5}\text{O}$  can act as a chemical anchor at the cathode in Li-S batteries, helping suppress the detrimental shuttle effect of dissolution lithium polysulfides.<sup>168</sup> Overall, the structural stability, high capacities, and cyclability lend HEO electrode materials great potential for further development.

### 9.1.2 | Catalysis

HEOs also show promise as prospective catalyst materials for various chemical reactions.<sup>11</sup> In  $\text{Mg}_{1/5}\text{Co}_{1/5}\text{Ni}_{1/5}\text{Cu}_{1/5}\text{Zn}_{1/5}\text{O}$ , Cu can undergo reversible redox between  $\text{Cu}^{2+}$  and  $\text{Cu}^+$ , enabling CO oxidation under favorable conditions.<sup>56</sup> Adding just 0.3 wt% Pt can drastically improve performance.<sup>73</sup> Entropy and disorder appear to mitigate detrimental clustering of active metals such as Pt or Pd, effectively resulting in single-atom catalysts.<sup>29,137</sup> Oxidized denary high-entropy nanoparticles exhibit high performance and stability as methane combustion catalysts.<sup>169</sup> In  $(\text{Mn}_{1/5}\text{Fe}_{1/5}\text{Co}_{1/5}\text{Ni}_{1/5}\text{Zn}_{1/5})\text{Fe}_2\text{O}_4$  catalysts, entropy appears to stabilize beneficial oxygen vacancies and active surface sites.<sup>115</sup> The  $(\text{Mg}_{1/4}\text{Fe}_{1/4}\text{Co}_{1/4}\text{Ni}_{1/4})\text{O}_x$  system shows a remarkable ability to facilitate thermochemical water splitting (TWS), owing to Fe redox between 2+ and 3+. The system takes a two-phase rocksalt-spinel phase structure. Upon heating, it produces  $\text{O}_2$  to increase the rocksalt fraction. Upon cooling, it can acquire oxygen from  $\text{H}_2\text{O}$  to increase the spinel fraction, producing  $\text{H}_2$  in the process. This facilitates robust  $\text{O}_2$  and  $\text{H}_2$  production at lower temperatures than other materials of interest for TWS.<sup>72</sup> This example combines the aforementioned ability to disperse active species (namely Fe) and also illustrates the potential for leveraging thermodynamically robust phase transformations associated with HEO systems.

## 9.2 | Magnetism

Since magnetic properties depend upon local magnetic exchange interactions, the local chemical disorder inherent to HEO systems results in complex and potentially tunable magnetic behavior, reviewed previously.<sup>13</sup> Local disorder can result in broad magnetic phase transitions and localized spin interactions that can persist above the macroscopic phase transition temperature.<sup>13</sup> Rocksalt,<sup>25</sup> perovskite,<sup>32,33,170</sup> and spinel<sup>26,81,82,145</sup> HEO systems show magnetic tunability via cation selection, giving HEOs potential as bespoke magnetic materials. Depending on cation selection, Néel temperatures can range from ~115 to 185 K in antiferromagnetic rare-earth-based perovskite

HEOs<sup>27</sup> and ~30 to 770 K in antiferromagnetic first-row transition metal spinel HEOs.<sup>26</sup> Experiments on rock-salt HEOs suggest magnetic ordering can even become frustrated to the point of generating a spin-glass ground state.<sup>25</sup>

$\text{Mg}_{1/5}\text{Co}_{1/5}\text{Ni}_{1/5}\text{Cu}_{1/5}\text{Zn}_{1/5}\text{O}$  was one of the first HEOs targeted for the purpose of understanding magnetic properties of HEOs. It exhibits long-range antiferromagnetic ordering with a Néel temperature around 110–120 K,<sup>25,79,141</sup> behaving as a type-II antiferromagnet, similar to NiO and CoO.<sup>25,79</sup> However, no structural transformation or anomaly in heat capacity coincident to the magnetic transition has been observed, contrasting simpler magnetically dilute oxide solutions.<sup>25,79</sup> Theoretical investigations indicate the onset of paramagnetism at nonmagnetic cation concentrations >84%, similar to  $\text{Co}_{1-x}\text{Mg}_x\text{O}$  and  $\text{Ni}_{1-x}\text{Mg}_x\text{O}$  solutions.<sup>80</sup>

In some  $\text{A}^{3+}\text{B}^{3+}\text{O}_3$  perovskite HEOs, researchers proposed competing AFM and FM ordering.<sup>27</sup> In  $(\text{Y}_{1/5}\text{La}_{1/5}\text{Nd}_{1/5}\text{Sm}_{1/5}\text{Gd}_{1/5})\text{XO}_3$  ( $\text{X} = \text{Co}, \text{Cr}, \text{or Fe}$ ), magnetic behavior appears largely controlled by the transition metal B-site magnetic moment interactions and d-orbital overlap, with magnetic rare-earth A-site cations contributing to local magnetic phase fluctuations.<sup>172</sup> Similarly, among the spinel compositions  $\text{XFe}_2\text{O}_4$ ,  $\text{XCr}_2\text{O}_4$ , and  $\text{XCo}_2\text{O}_4$  (where X is an equimolar collection of five of: Mg, Mn, Fe, Co, Ni, Cu, or Zn), choice of B-site cation strongly influenced total magnetic behavior. Notably, the ferrites exhibit high-temperature ferrimagnetism.<sup>26</sup>

Regarding the equimolar ferrimagnetic spinel  $(\text{Cr}_{1/5}\text{Mn}_{1/5}\text{Fe}_{1/5}\text{Co}_{1/5}\text{Ni}_{1/5})_3\text{O}_4$ , substituting nonmagnetic  $\text{Zn}^{2+}$  for  $\text{Co}^{2+}$  or  $\text{Ni}^{2+}$  in  $(\text{Cr}_{1/5}\text{Mn}_{1/5}\text{Fe}_{1/5}\text{Co}_{1/5}\text{Ni}_{1/5})_3\text{O}_4$  weakens magnetic ordering and decreases magnetization.<sup>82</sup>  $\text{Ga}^{3+}$  incorporation up to 40% can be accommodated by valence and lattice site reorganizations for Mn, Fe, and Co, resulting in a suppression of magnetic ordering temperature and change in magnetic ground state.<sup>81</sup> These examples highlight the importance of cation selection as a design principle for tuning magnetic ordering and strength.

Single crystal and epitaxial HEO reports provide additional magnetic insight. Epitaxial  $\text{Mg}_{1/5}\text{Co}_{1/5}\text{Ni}_{1/5}\text{Cu}_{1/5}\text{Zn}_{1/5}\text{O}$ -related heterostructures show large and tunable magnetic exchange biases.<sup>67,116,120</sup> Epitaxial strain tuning has been applied to alter magnetic texture in  $(\text{Mg}_{1/5}\text{Fe}_{1/5}\text{Co}_{1/5}\text{Ni}_{1/5}\text{Cu}_{1/5})\text{Fe}_2\text{O}_4$ <sup>151</sup> and magnetic anisotropy in  $\text{La}(\text{Cr}_{1/5}\text{Mn}_{1/5}\text{Fe}_{1/5}\text{Co}_{1/5}\text{Ni}_{1/5})\text{O}_3$ .<sup>149</sup> Bulk  $(\text{Gd}_{1/5}\text{Tb}_{1/5}\text{Dy}_{1/5}\text{Er}_{1/5}\text{Yb}_{1/5})_2\text{Ti}_2\text{O}_7$  single crystals exhibit strong evidence for a spin-glass ground state.<sup>95</sup> Although not an oxide compound, bulk single crystals of  $(\text{Gd}_{0.38}\text{Tb}_{0.27}\text{Dy}_{0.20}\text{Ho}_{0.15})\text{Mn}_6\text{Sn}_6$  kagome magnets exhibit multiple spin reorientation transitions, enable by entropy and disorder, further demonstrating how the

high-entropy condition can strongly influence magnetic properties.<sup>173</sup>

Epitaxial  $\text{La}(\text{Cr}_{1/5}\text{Mn}_{1/5}\text{Fe}_{1/5}\text{Co}_{1/5}\text{Ni}_{1/5})\text{O}_3$  and related compositions have proven a useful for studying spin, charge, and oxygen-mediated coupling between different transition metal cations compared to individual end-member magnetic perovskites.<sup>110,174</sup>  $\text{La}(\text{Cr}_{1/5}\text{Mn}_{1/5}\text{Fe}_{1/5}\text{Co}_{1/5}\text{Ni}_{1/5})\text{O}_3$  films appear to exhibit competing local antiferromagnetic and ferromagnetic clusters, but substituting Sr(formally 2+) for La (formally 3+) at concentrations of around 30% or more forces charge redistribution and causes these local clusters to couple magnetically.<sup>110</sup> Combined experiment and Monte Carlo simulations employing a simple Heisenberg model captured the effects of varying Mn concentration in  $\text{La}(\text{Mn}_x\text{Cr}_{(1-x)/4}\text{Fe}_{(1-x)/4}\text{Co}_{(1-x)/4}\text{Ni}_{(1-x)/4})\text{O}_3$  compared to end-member magnetic perovskites.<sup>174</sup> At 40% Mn, ferromagnetic and antiferromagnetic regions appear coherent over long distances and beyond 50% Mn, antiferromagnetic clusters become embedded in a percolated ferromagnetic matrix.<sup>174</sup> Substituting Tb for La in  $\text{La}(\text{Cr}_{1/5}\text{Mn}_{1/5}\text{Fe}_{1/5}\text{Co}_{1/5}\text{Ni}_{1/5})\text{O}_3$  results in similar complex multiphase magnetic ordering but a larger fraction of soft switchable magnetic moments.<sup>175</sup>

Along with unique magnetic tunability, manipulating the local spin disorder chemically may drive local magnetic exchange, charge transfer, and other behaviors more commonly achieved at interfaces in deliberate thin film heterostructures.<sup>174,176</sup> Overall, HEOs serve as useful models for studying and controlling frustrated macroscopic magnetic ordering and frustration-driven dynamic spin interactions. Because of the high degree of site-to-site spin and exchange type inhomogeneity, HEOs offer a potential avenue for continuous control over magnetic ordering types and critical temperatures. Understanding the magnetic phase transformations in magnetic HEOs may benefit from application of Landau theory in the future, which explicitly relates thermodynamics and free energy to order parameters in the vicinity of a phase transformation.

### 9.3 | Ionic and electronic transport properties

The extrapolated oxygen diffusion coefficient in  $\text{Mg}_{1/5}\text{Co}_{1/5}\text{Ni}_{1/5}\text{Cu}_{1/5}\text{Zn}_{1/5}\text{O}$  at 900°C is low compared to CoO and NiO but falls within the general range of expected for transition metal oxides.<sup>77</sup> In Li-modified  $\text{Mg}_{1/5}\text{Co}_{1/5}\text{Ni}_{1/5}\text{Cu}_{1/5}\text{Zn}_{1/5}\text{O}$ , ionic conductivity is likely aided by extrinsic oxygen vacancies produced upon Li inclusion,<sup>65,76</sup> with ionic conductivity tending to increase upon increasing the Li concentration as more oxygen

vacancies are formed. Early reports claimed nearly pure ionic transport,<sup>65</sup> but more recent characterization suggests complex mixed electronic-ionic conduction mechanisms.<sup>133,177</sup> Improved alkali ion conductivity has been demonstrated in phosphate Na super-ionic conductor frameworks and Li-garnet frameworks by combining configurational entropy with an alkali metal-stuffing strategy that forces alkali ions to occupy higher-energy lattice sites.<sup>83</sup> Other works on ion conduction include high-entropy Ba-based perovskite proton conductors<sup>178</sup> but no improvement over conventional materials was observed. Ionic conductivity in fluorite  $(\text{Zr}_{1/3}\text{Ce}_{1/3}\text{Hf}_{1/3})_{1-x}(\text{Y}_{1/2}\text{Gd}_{1/2})_x\text{O}_{2-\delta}$  systems with x ranging from 0.16 to 0.60 did not exceed  $4 \times 10^{-4} \text{ S cm}^{-1}$  at 600°C, the target value for SOFC applications.<sup>179</sup>

HEO systems can exhibit insulating, metallic, or semiconducting electronic behavior. Semiconducting behavior is sometimes attributed to polaron hopping,<sup>117,152,170</sup> or mixed ionic-electronic conductivity.<sup>117,165,177</sup> An illustrative example is Mo-containing fluorite HEOs, where charge hopping between  $\text{Pr}^{3+}$  and  $\text{Pr}^{4+}$  likely occurs at low temperatures, whereas ionic transport is activated at elevated temperatures.<sup>117</sup> The entropic distribution of Fe in  $(\text{Mg}_{1/5}\text{Fe}_{1/5}\text{Ni}_{1/5}\text{Zn}_{1/5}\text{Cd}_{1/5})\text{Fe}_2\text{O}_4$  appears to impede electron hopping between Fe ions relative to simple ferrites, resulting in relatively suppressed electron transport.<sup>139</sup> Compositionally tunable conductivity was demonstrated in a series of mixed-phase rocksalt-spinel films; higher Mn concentrations correlating to lower resistivity.<sup>154</sup>

Metallic conduction has been observed in  $(\text{La}_{1/5}\text{Pr}_{1/5}\text{Nd}_{1/5}\text{Sm}_{1/5}\text{Eu}_{1/5})_2\text{CuO}_4$  cuprate thin films, but a superconducting phase transition was not observed.<sup>39</sup>  $\text{REBa}_2\text{Cu}_3\text{O}_{7-\delta}$  HEOs do however appear to exhibit a superconducting phase transition at 92 K, similar to  $\text{YBa}_2\text{Cu}_3\text{O}_{7-\delta}$ .<sup>180</sup> Intriguing electron-correlated phenomena have been observed in some HEO systems.  $(\text{Y}_{1/5}\text{La}_{1/5}\text{Nd}_{1/5}\text{Sm}_{1/5}\text{Gd}_{1/5})\text{CoO}_3$  experiences a decrease in electronic bandgap below ~240 K, coincident with a magnetic phase transition.<sup>181</sup> Epitaxial  $(\text{La}_{1/5}\text{Pr}_{1/5}\text{Nd}_{1/5}\text{Sm}_{1/5}\text{Eu}_{1/5})\text{NiO}_3$  films exhibit metallic conduction and a metal-insulator transition between ~170 and 190 K when grown on  $\text{NdGaO}_3$  substrates by PLD<sup>34</sup> and between ~100 and 150 K when grown on variously-oriented  $\text{LaAlO}_3$  substrates by a sol-gel method.<sup>146</sup>  $(\text{La}_{1/4}\text{Nd}_{1/4}\text{Sm}_{1/4}\text{Gd}_{1/4})_{1-x}\text{Sr}_x\text{MnO}_3$ , with varying amounts of Sr as a hole dopant demonstrate a complex magneto-electronic phase diagram with unique temperature dependencies.  $(\text{La}_{1/4}\text{Nd}_{1/4}\text{Sm}_{1/4}\text{Gd}_{1/4})_{7/10}\text{Sr}_{3/10}\text{MnO}_3$  exhibits colossal magnetoresistance of 1550% stemming from a metal-insulator transition at 123 K, matching the best-known values for bulk conventional manganites.<sup>182</sup> The possibility of compositionally tuning such electron-correlated behavior may facilitate a deeper



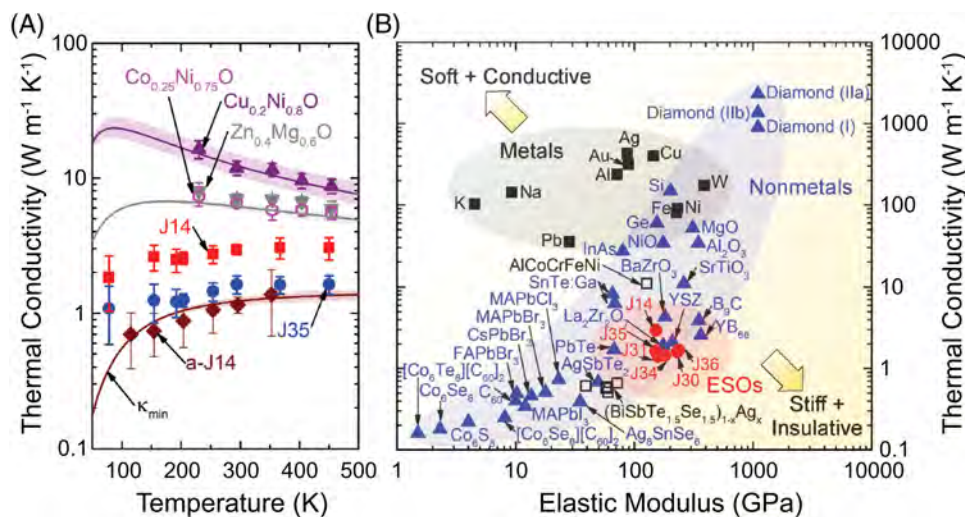


**FIGURE 8** Thermal and mechanical characterization of  $\text{Mg}_{1/5}\text{Co}_{1/5}\text{Ni}_{1/5}\text{Cu}_{1/5}\text{Zn}_{1/5}\text{O}$  (J14) and  $\text{Mg}_{1/6}\text{Co}_{1/6}\text{Ni}_{1/6}\text{Cu}_{1/6}\text{Zn}_{1/6}\text{X}_{1/6}\text{O}$  ( $\text{X} = \text{Sc}, \text{Sb}, \text{Sn}, \text{Cr}, \text{or Ge}$ ; J30, J31, J34, J35, or J36 respectively): (A) thermal conductivity as a function of temperature where a-J14 is amorphous J14 and  $\kappa_{\min}$  is the minimum model for J14; and (B) thermal and elastic properties of crystals. *Source:* Adapted from Ref. 24 with permission; copyright 2018 WILEY-VCH Verlag GmbH & Co. KGaA, Weinheim. Sources used to construct part (B) are also provided in Ref. 24.

understanding of correlated phenomena in disordered crystals.

## 9.4 | Thermal conductivity, hardness, and thermoelectricity

A notable property intrinsic to HEOs is low thermal conductivity, owing to structural and electronic disorder that disrupts phonon transport. Thermal analysis of epitaxial  $\text{Mg}_{1/5}\text{Co}_{1/5}\text{Ni}_{1/5}\text{Cu}_{1/5}\text{Zn}_{1/5}\text{O}$  and six-component derivatives indicate thermal conductivities below 1.5 W/m K, approaching that of amorphous  $\text{Mg}_{1/5}\text{Co}_{1/5}\text{Ni}_{1/5}\text{Cu}_{1/5}\text{Zn}_{1/5}\text{O}$ <sup>24</sup>, shown in Figure 8. Similarly, systematic studies of  $\text{X}_3\text{NbO}_7$  (where X is an equimolar collection selected from: Sm, Eu, Gd, Dy, Ho, and Er) HEOs reveal low thermal conductivities compared to simpler niobates.<sup>90</sup> Both of these studies show that mechanical strength can be maintained or improved as thermal conductivity is reduced.<sup>24,90</sup> The elastic modulus of  $\text{Mg}_{1/5}\text{Co}_{1/5}\text{Ni}_{1/5}\text{Cu}_{1/5}\text{Zn}_{1/5}\text{O}$  increases by around 50% upon the equimolar inclusion of Sc, giving it one of the highest ratios of elastic modulus to thermal conductivity for any isotropic crystal.<sup>24</sup>

The ability to combine low thermal conductivity with uncompromised mechanical properties led to interest in perovskite,<sup>134</sup> fluorite,<sup>91,92</sup> pyrochlore,<sup>38</sup> silicate,<sup>41,42,144</sup> and phosphate<sup>44</sup> HEOs for thermal barrier coatings. For example, high-entropy disilicates show promise for protecting SiC-based composites<sup>144</sup> and aluminate perovskites show promise for protecting  $\text{Al}_2\text{O}_3$ -based composites.<sup>134</sup>

Additionally, inherently low HEO thermal conductivities and potential for semiconducting electrical behavior naturally led to investigation of thermoelectricity in HEOs.  $(\text{Ca}_{1/5}\text{Sr}_{1/5}\text{Ba}_{1/5}\text{La}_{1/5}\text{Pb}_{1/5})\text{TiO}_3$  ceramics achieved  $zT$  values of  $\sim 0.2$  at elevated temperature,<sup>93</sup> indicating that decreasing thermal conductivity via disorder is a promising route for oxide thermoelectric development.

## 9.5 | Dielectric properties

Early dielectric characterization of  $\text{Mg}_{1/5}\text{Co}_{1/5}\text{Ni}_{1/5}\text{Cu}_{1/5}\text{Zn}_{1/5}\text{O}$  and derived rocksalts showed large permittivities, in excess of 1000, at frequencies above the kHz range. Notably, the permittivity is tunable via Li concentration, with increased Li concentrations decreasing low-frequency permittivity and generating an additional feature in the dispersion.<sup>66</sup> Large loss tangents at low frequencies and high temperatures indicate space charge contributions, potentially from mixed ionic–electronic conductivity in related materials.<sup>177</sup> These early observations prompted further development of HEO dielectrics.

HEO researchers quickly turned to the perovskite structural class in the search for dielectric functionality. Cubic  $\text{Ba}(\text{Ti}_{1/5}\text{Zr}_{1/5}\text{Sn}_{1/5}\text{Hf}_{1/5}\text{X}_{1/5})\text{O}_3$  ( $\text{X} = \text{V}, \text{Y}, \text{Nb}, \text{Mo}, \text{Ta}, \text{or W}$ ) systems exhibit a high degree of tunability, with permittivities ranging from about 50 to 130.<sup>183</sup> Some high-entropy titanate perovskite HEOs exhibit frequency-dispersive relaxor-like ferroelectric behavior<sup>84–86,184</sup> ( $\text{Na}_{1/5}\text{Bi}_{1/5}\text{Ca}_{1/5}\text{Sr}_{1/5}\text{Ba}_{1/5}\text{TiO}_3$  ceramic permittivities reach a maximum over 2000 between



about 25 and 75°C, depending on frequency,<sup>84</sup> whereas  $(\text{Na}_{1/5}\text{K}_{1/5}\text{Bi}_{1/5}\text{Ca}_{1/5}\text{Ba}_{1/5})\text{TiO}_3$  permittivities reach a reported maximum over 1200 at around 250°C,<sup>85</sup> revealing an ability to tune phase transition temperature based on cation selection, similar to magnetic HEOs and more traditional ferroelectric systems. Relaxor-like behavior was observed in the  $(\text{Ca}_{1/4}\text{Sr}_{1/4}\text{Ba}_{1/4}\text{Pb}_{1/4})\text{TiO}_3$  system as well, with a permittivity maximum over 10000 around 60°C before poling, dropping to just over 3500 after poling,<sup>86</sup> suggesting a polarizability increase from Pb inclusion. The high-entropy concept was extended to Aurivillius phase relaxors, which can exhibit a higher freezing temperature than end-member phases.<sup>185</sup> Early observations of high piezoelectric responses<sup>185,186</sup> generate further intrigue in the realm of ferroelectric and piezoelectric HEO development.

Further development of nonlinear dielectric HEOs is no doubt on the horizon. A property of particular interest is electrocaloric activity, which relates entropy and temperature change in a crystal.<sup>187</sup> The disorder and entropy associated with HEO atomic configurations may frustrate the formation of large ferroelectric domains, similar to traditional relaxor ferroelectrics, and result in a large electronic and dipolar entropy change upon application of external fields, resulting in large entropy changes and a large electrocaloric coefficient.  $(\text{Na}_{1/5}\text{Bi}_{1/5}\text{Ca}_{1/5}\text{Sr}_{1/5}\text{Ba}_{1/5})\text{TiO}_3$  electrocaloric activity was calculated, with a maximum temperature change of 0.63 K near 40°C; higher than similar, lower entropy lead-free ceramics.<sup>84</sup> Inherent compositional flexibility should provide ample opportunity to explore composition space in an effort to control dipole interaction lengths, order parameters, and dielectric relaxation times. As with magnetic HEOs, a fruitful route of study may be application of Landau theory<sup>188</sup> to analyze ferroelectric HEO phase transformations and elucidate the influence of chemical disorder, ferroelectric order parameters, and thermodynamics.

## 9.6 | Optical tunability

Preliminary optical absorption and tunability has been studied for the  $\text{Mg}_{1/5}\text{Co}_{1/5}\text{Ni}_{1/5}\text{Cu}_{1/5}\text{Zn}_{1/5}\text{O}$  and  $\text{Y}_{1/5}\text{La}_{1/5}\text{Ce}_{1/5}\text{Pr}_{1/5}\text{Sm}_{1/5}\text{O}_{2-\delta}$  families of HEOs. Concerning  $\text{Mg}_{1/5}\text{Co}_{1/5}\text{Ni}_{1/5}\text{Cu}_{1/5}\text{Zn}_{1/5}\text{O}$ , early optical models suggest multiple, overlapping and relatively broad absorption features across the visible spectrum.<sup>116</sup> The number and width of the features may be a reflection of localized electronic disorder. Inducing a Co valence change from majority 2+ to a mix of 2+ and 3+, either by growing films in relatively oxidizing conditions<sup>116</sup> or introducing  $\text{Li}^+$  to the crystal<sup>66,76</sup>, increases absorbance at visible frequencies.

In terms of cation selection, compositionally tunable bandgaps are nicely demonstrated in  $\text{CeO}_2$ -based HEO systems, correlating strongly to Pr concentration, since Pr multivalency produces low-lying electronic states.<sup>23</sup> Additionally, the net Pr and Tb valences state in  $\text{Y}_{1/5}\text{La}_{1/5}\text{Ce}_{1/5}\text{Pr}_{1/5}\text{Sm}_{1/5}\text{O}_{2-\delta}$  or similar fluorite-derived HEOs is tunable via  $p\text{O}_2$  modulation, with an associated optical bandgap shift.<sup>102,189</sup> Leveraging potentially small bandgaps and broadband absorption gives HEOs applicability in the realm of photocatalysis<sup>190,191</sup> and potentially solar energy harvesting.

HEOs can also act as a host lattice for optically active cations. High-entropy sesquioxides containing Dy and Yb exhibit multiwavelength photon emission coincident with transparency,<sup>192</sup> and  $\text{Eu}^{3+}$ -doped  $\text{Zr}_{1/5}\text{La}_{1/5}\text{Ce}_{1/5}\text{Gd}_{1/5}\text{Hf}_{1/5}\text{O}_{2-\delta}$  exhibits luminescent properties.<sup>111</sup> Considering the aforementioned potential for ferroelectricity, development of nonlinear optical HEOs is also an intriguing area of future work.

## 9.7 | Radiation protection

Local disorder and possible incorporation of heavy elements give HEOs potential as shielding materials against damaging radiation. A composite of epoxy and  $(\text{La}_{1/5}\text{Ce}_{1/5}\text{Gd}_{1/5}\text{Er}_{1/5}\text{Tm}_{1/5})_2(\text{WO}_4)_3$  powders exhibit remarkable thermal neutron and gamma radiation shielding properties. The high neutron and gamma ray attenuation owes to the distribution of heavy nuclei and 4f valence orbitals.<sup>193</sup> Additionally,  $(\text{Eu}_{1-x}\text{Gd}_x)_2(\text{Ti}_{1/5}\text{Zr}_{1/5}\text{Nb}_{1/5}\text{Ce}_{1/5}\text{Hf}_{1/5})_2\text{O}_7$  pyrochlore ceramics (with a minor fluorite impurity phase) exhibit improved performance over simpler pyrochlores in immobilizing high-level radioactive waste. In this case, lattice distortion and a low oxygen vacancy concentration serve to limit leaching.<sup>194</sup> Given these early observations, potential HEO implementation as protection against hazardous material is a fruitful route for future development.

## 9.8 | Elastic and high-pressure behavior

Elastic property studies on  $\text{Mg}_{1/5}\text{Co}_{1/5}\text{Ni}_{1/5}\text{Cu}_{1/5}\text{Zn}_{1/5}\text{O}$  suggest bulk and shear moduli values within the range predicted by a rule of mixtures, but a high Pugh ratio that suggests ductile behavior. Distortions around Cu and Zn appear to promote isotropic elastic behavior.<sup>130</sup> Hydrostatic high-pressure studies of  $\text{Mg}_{1/5}\text{Co}_{1/5}\text{Ni}_{1/5}\text{Cu}_{1/5}\text{Zn}_{1/5}\text{O}$  indicate rigid first-neighbor interactions up to ~9 GPa but severe structural distortion at higher pressures without observable symmetry-breaking or phase transformations. This critical pressure corresponds roughly to the

wurtzite–rocksalt ZnO transformation,<sup>195</sup> suggesting that local bond stabilities influence the onset of lattice distortion. Accordingly, light Li- or Mn-doping decreases the bulk modulus, due to the relatively weak Li–O and Mn–O bonding interactions.<sup>109</sup>  $\text{Y}_{1/5}\text{La}_{1/5}\text{Ce}_{1/5}\text{Pr}_{1/5}\text{Sm}_{1/5}\text{O}_{2-\delta}$  exhibits a slightly different high-pressure behavior. Upon hydrostatic pressure application, severe lattice distortion develops continuously until the structure becomes amorphous around 20 GPa. The first-near neighbor bonds in  $\text{Y}_{1/5}\text{La}_{1/5}\text{Ce}_{1/5}\text{Pr}_{1/5}\text{Sm}_{1/5}\text{O}_{2-\delta}$  retain rigidity, but oxygen vacancies appear to change coordination and facilitate amorphization. Upon recovery, nanocrystals nucleate in the amorphous matrix.<sup>196</sup> As with nearly all HEO properties, the combination of compositional flexibility and local disorder can be controlled to alter net mechanical behavior.

## 10 | CONCLUSIONS AND OUTLOOK

Configurational entropy engineering, adopted from the metallurgy community, quickly prompted an exponential expansion of accessible oxide chemical compositions. Two inherent HEO attributes generate intrigue among the oxide community: compositional flexibility awarded by entropy-driven solution formation and local disorder from complex stoichiometries. These attributes manifest in controllable localized phenomena that impact macroscopic properties, distinguishing HEOs from simpler oxide compounds and solutions.

HEOs are predominantly high-temperature phases and tend toward metastability at ambient conditions. Phase formation requires simulating equilibrium stability conditions or employing nonequilibrium synthesis techniques with facile kinetic pathways for solution nucleation. After quenching, HEO solid solutions typically decompose too slowly to observe at ambient conditions. At intermediate temperatures, however, structural relaxation toward equilibrium can occur on experimental timescales, resulting in nonrandom atomic configurations or microstructures. Future avenues for HEO engineering may include harnessing kinetics to control phase structures and domain structures; or engineering composite nanostructures and thin film heterostructures.

Standout HEO properties include electrochemical utility, low thermal conductivity, unique magnetic phase structures, relaxor ferroelectricity, and electrocaloric activity. Synergy between compositional flexibility, entropic cation distributions, and microstructural stability result in remarkable potential as energy materials and catalysts. Local asymmetry can manifest in locally frustrated magnetic ordering, suppressed phonon transport, or dispersive dielectric relaxation facilitating relaxor ferroelec-

tricity. Compositional flexibility results in tunable properties, such as magnetic ordering temperatures, dielectric constant dispersions, and thermal transport. Some property combinations that facilitate engineering functionality include: low thermal conductivity, uncompromised mechanical properties, and high-temperature stability; low thermal conductivity and semiconducting behavior; and broad optical absorption features combined with semiconducting behavior. Coincident local disorder and compositional tunability also make HEO systems excellent platforms for understanding electron-correlated phenomena in complex crystals.


The advent of entropy engineering comes at an exciting time in human history. A century ago, advances in modern physics enabled a quantum understanding of material properties. Computing technology enabled materials simulations and high-throughput predictive capacities, facilitating novel materials discovery. With modern consumer microelectronics and wireless connectivity, knowledge acquisition and transmission are easier than ever. The advent of HEAs proved that we are far from exhausting all possible combinations of elements on the periodic table. Now, with the extension of entropy engineering to ceramics, materials researchers can rejoice knowing a multitude of new materials await discovery, characterization, and implementation.


## ACKNOWLEDGMENTS

G.N.K. and J.-P.M. gratefully acknowledge support from NSF ceramics Award No. DMR-1610844 and NSF Award No. DMR-1839087. G.N.K., S.S.I.A., F.M.S.V., I.D., C.M.R., V.H.C., and J.-P.M. gratefully acknowledge support from NSF MRSEC DMR-2011839. The authors would also like to acknowledge many helpful and enlightening discussions with Susan Trolier-McKinstry, Long-Qing Chen, John T. Heron, Susan B. Sinnott, Venkatraman Gopalan, Nasim Alem, and Zhiqiang Mao regarding the nuances of high-entropy systems.

## ORCID

George N. Kotsonis  <https://orcid.org/0000-0003-2939-0746>

Saeed S. I. Almishal  <https://orcid.org/0000-0003-2964-6000>

Christina M. Rost  <https://orcid.org/0000-0002-6153-6066>

Jon-Paul Maria  <https://orcid.org/0000-0003-3604-4761>

## REFERENCES

1. Cantor B, Chang ITH, Knight P, Vincent AJB. Microstructural development in equiatomic multicomponent alloys. *Mater Sci Eng, A*. 2004;375–377(1–2 SPEC. ISS.):213–8. <https://doi.org/10.1016/j.msea.2003.10.257>

2. Yeh J-W, Chen S-K, Lin S-J, Gan J-Y, Chin T-S, Shun T-T, et al. Nanostructured high-entropy alloys with multiple principal elements: novel alloy design concepts and outcomes. *Adv Eng Mater.* 2004;6(5):299. <https://doi.org/10.1002/adem.200300567>
3. Rost CM, Sachet E, Borman T, Moballegh A, Dickey EC, Hou D, et al. Entropy-stabilized oxides. *Nat Commun.* 2015;6:8485. <https://doi.org/10.1038/ncomms9485>
4. Miracle DB, Senkov ON. A critical review of high entropy alloys and related concepts. *Acta Mater.* 2017;122:448–511. <https://doi.org/10.1016/j.actamat.2016.08.081>
5. Musicó BL, Yan J, Gilbert D, Ward TZ, Page K, George E, et al. The emergent field of high entropy oxides: design, prospects, challenges, and opportunities for tailoring material properties. *Appl Phys Lett Mater.* 2020;8:040912. <https://doi.org/10.1063/5.0003149>
6. Salián A, Mandal S. Entropy stabilized multicomponent oxides with diverse functionality – a review. *Crit Rev Solid State Mater Sci.* 2021;47(2):142–93. <https://doi.org/10.1080/10408436.2021.1886047>
7. Oses C, Toher C, Curtarolo S. High-entropy ceramics. *Nat Rev Mater.* 2020;5:295–309. <https://doi.org/10.1038/s41578-019-0170-8>
8. Zhang R-Z, Reece MJ. Review of high entropy ceramics: design, synthesis, structure and properties. *J Mater Chem A.* 2019;7(39):22148–62. <https://doi.org/10.1039/C9TA05698J>
9. Xiang H, Xing Y, Dai F, Wang H, Su L, Miao L, et al. High-entropy ceramics: present status, challenges, and a look forward. *J Adv Ceram.* 2021;10(3):385–441. <https://doi.org/10.1007/s40145-021-0477-y>
10. Chen Y, Fu H, Huang Y, Huang L, Zheng X, Dai Y, et al. Opportunities for high-entropy materials in rechargeable batteries. *ACS Mater Lett.* 2021;3(2):160–70. <https://doi.org/10.1021/acsmaterialslett.0c00484>
11. Albedwawi SH, AlJaberi A, Haidemenopoulos GN, Polychronopoulou K. High entropy oxides-exploring a paradigm of promising catalysts: a review. *Mater Des.* 2021;202:109534. <https://doi.org/10.1016/j.matdes.2021.109534>
12. Sun Y, Dai S. High-entropy materials for catalysis: a new frontier. *Sci Adv.* 2021;7(20):eabg1600. <https://doi.org/10.1126/sciadv.abg1600> PMID: 33980494
13. Sarkar A, Kruk R, Hahn H. Magnetic properties of high entropy oxides. *Dalton Trans.* 2021;50(6):1973–82. <https://doi.org/10.1039/D0DT04154H>
14. Simonov A, Goodwin AL. Designing disorder into crystalline materials. *Nat Rev Chem.* 2020;4(12):657–73. <https://doi.org/10.1038/s41570-020-00228-3> PMID: 3712977
15. Djenadic R, Sarkar A, Clemens O, Loho C, Botros M, Chakravadhanula VSK, et al. Multicomponent equiatomic rare earth oxides. *Mater Res Lett.* 2017;5(2):102–9. <https://doi.org/10.1080/21663831.2016.1220433>
16. Pianassola M, Loveday M, McMurray JW, Koschan M, Melcher CL, Zhuravleva M. Solid-state synthesis of multicomponent equiatomic rare-earth oxides. *J Am Ceram Soc.* 2020;103(4):2908–18. <https://doi.org/10.1111/jace.16971>
17. Dąbrowa J, Stygar M, Mikuła A, Knapik A, Mroccka K, Tejchman W, et al. Synthesis and microstructure of the (Co,Cr,Fe,Mn,Ni)<sub>3</sub>O<sub>4</sub> high entropy oxide characterized by spinel structure. *Mater Lett.* 2018;216:32–6. <https://doi.org/10.1016/j.matlet.2017.12.148>
18. McCormack SJ, Navrotsky A. Thermodynamics of high entropy oxides. *Acta Mater.* 2021;202:1–21. <https://doi.org/10.1016/j.actamat.2020.10.043>
19. Dippo OF, Vecchio KSA. Universal configurational entropy metric for high-entropy materials. *Scr Mater.* 2021;201:113974. <https://doi.org/10.1016/j.scriptamat.2021.113974>
20. Wright AJ, Luo J. A step forward from high-entropy ceramics to compositionally complex ceramics: a new perspective. *J Mater Sci.* 2020;55(23):9812–27. <https://doi.org/10.1007/s10853-020-04583-w>
21. Styer DF. Insight into entropy. *Am J Phys.* 2000;68(12):1090–6. <https://doi.org/10.1119/1.1287353>
22. Kotsonis GN, Rost CM, Harris DT, Maria JP. Epitaxial entropy-stabilized oxides: growth of chemically diverse phases via kinetic bombardment. *MRS Commun.* 2018;8(3):1371–7. <https://doi.org/10.1557/mrc.2018.184>
23. Sarkar A, Loho C, Velasco L, Thomas T, Bhattacharya SS, Hahn H, et al. Multicomponent equiatomic rare earth oxides with a narrow band gap and associated praseodymium multivalency. *Dalton Trans.* 2017;46(36):12167–76. <https://doi.org/10.1039/c7dt02077e> PMID: 28869641
24. Braun JL, Rost CM, Lim M, Giri A, Olson DH, Kotsonis GN, et al. Charge-induced disorder controls the thermal conductivity of entropy-stabilized oxides. *Adv Mater.* 2018;30(51):1805004. <https://doi.org/10.1002/adma.201805004>
25. Jimenez-Segura MP, Takayama T, Bérardan D, Hosier A, Reehuis M, Takagi H, et al. Long-range magnetic ordering in rocksalt-type high-entropy oxides. *Appl Phys Lett.* 2019;114:122401. <https://doi.org/10.1063/1.5091787>
26. Musicó B, Wright Q, Ward TZ, Grutter A, Arenholz E, Gilbert D, et al. Tunable magnetic ordering through cation selection in entropic spinel oxides. *Phys Rev Mater.* 2019;3:104416. <https://doi.org/10.1103/PhysRevMaterials.3.104416>
27. Witte R, Sarkar A, Kruk R, Eggert B, Brand RA, Wende H, et al. High-entropy oxides: an emerging prospect for magnetic rare-earth transition metal perovskites. *Phys Rev Mater.* 2019;3(3):034406. <https://doi.org/10.1103/PhysRevMaterials.3.034406>
28. Sarkar A, Velasco L, Wang D, Wang Q, Talasila G, de Biasi L, et al. High entropy oxides for reversible energy storage. *Nat Commun.* 2018;9:3400. <https://doi.org/10.1038/s41467-018-05774-5> PMID: 30143625
29. Xu H, Zhang Z, Liu J, Do-Thanh CL, Chen H, Xu S, et al. Entropy-stabilized single-atom Pd catalysts via high-entropy fluorite oxide supports. *Nat Commun.* 2020;11(1):3908. <https://doi.org/10.1038/s41467-020-17738-9> PMID: 32764539
30. Gild J, Samiee M, Braun JL, Harrington T, Vega H, Hopkins PE, et al. High-entropy fluorite oxides. *J Eur Ceram Soc.* 2018;38:3578–84. <https://doi.org/10.1016/j.jeurceramsoc.2018.04.010>
31. Jiang S, Hu T, Gild J, Zhou N, Nie J, Qin M, et al. A new class of high-entropy perovskite oxides. *Scr Mater.* 2018;142:116–20. <https://doi.org/10.1016/j.scriptamat.2017.08.040>
32. Sarkar A, Djenadic R, Wang D, Hein C, Kautenburger R, Clemens O, et al. Rare earth and transition metal based entropy stabilised perovskite type oxides. *J Eur Ceram Soc.* 2018;38(5):2318–27. <https://doi.org/10.1016/j.jeurceramsoc.2017.12.058>
33. Cedervall J, Clulow R, Boström HLB, Joshi DC, Andersson MS, Mathieu R, et al. Phase stability and structural transi-

- tions in compositionally complex  $\text{LnMO}_3$  perovskites. *J Solid State Chem.* 2021;300(April):122213. <https://doi.org/10.1016/j.jssc.2021.122213>
34. Patel RK, Ojha SK, Kumar S, Saha A, Mandal P, Freeland JW, et al. Epitaxial stabilization of ultra thin films of high entropy perovskite. *Appl Phys Lett.* 2020;116:071601. <https://doi.org/10.1063/1.5133710>
  35. Chen TY, Wang SY, Kuo CH, Huang SC, Lin MH, Li CH, et al. In operando synchrotron X-ray studies of a novel spinel ( $\text{Ni}_{0.2}\text{Co}_{0.2}\text{Mn}_{0.2}\text{Fe}_{0.2}\text{Ti}_{0.2}$ ) $_3\text{O}_4$  high-entropy oxide for energy storage applications. *J Mater Chem A.* 2020;8(41):21756–70. <https://doi.org/10.1039/d0ta06455f>
  36. Fracchia M, Manzoli M, Anselmi-Tamburini U, Ghigna P. A new eight-cation inverse high entropy spinel with large configurational entropy in both tetrahedral and octahedral sites: synthesis and cation distribution by X-ray absorption spectroscopy. *Scr Mater.* 2020;188:26–31. <https://doi.org/10.1016/j.scriptamat.2020.07.002>
  37. Jiang B, Bridges CA, Unocic RR, Pitike KC, Cooper VR, Zhang Y, et al. Probing the local site disorder and distortion in pyrochlore high-entropy oxides. *J Am Chem Soc.* 2021;143(11):4193–204. <https://doi.org/10.1021/jacs.0c10739> PMID: 33352040
  38. Wright AJ, Wang Q, Ko S-T, Chung KM, Chen R, Luo J. Size disorder as a descriptor for predicting reduced thermal conductivity in medium- and high-entropy pyrochlore oxides. *Scr Mater.* 2020;181:76–81. <https://doi.org/10.1016/j.scriptamat.2020.02.011>
  39. Mazza AR, Gao X, Rossi DJ, Musico BL, Valentine TW, Kennedy Z, et al. Searching for superconductivity in high entropy oxide Ruddlesden-Popper cuprate films. *J Vac Sci Technol A.* 2022;40(1):013404. <https://doi.org/10.1116/6.0001441>
  40. Chen H, Xiang H, Dai F-Z, Liu J, Zhou Y. High entropy ( $\text{Yb}_{0.25}\text{Y}_{0.25}\text{Lu}_{0.25}\text{Er}_{0.25}$ ) $_2\text{SiO}_5$  with strong anisotropy in thermal expansion. *J Mater Sci Technol.* 2020;36:134–9. <https://doi.org/10.1016/j.jmst.2019.07.022>
  41. Salanova A, Brummel IA, Yakovenko AA, Opila EJ, Ihlefeld JF. Phase stability and tensorial thermal expansion properties of single to high-entropy rare-earth disilicates. *J Am Ceram Soc.* 2023;106(5):3228–38. <https://doi.org/10.1111/jace.18986>
  42. Ren X, Tian Z, Zhang J, Wang J. Equiatomic quaternary ( $\text{Y}_{1/4}\text{Ho}_{1/4}\text{Er}_{1/4}\text{Yb}_{1/4}$ ) $_2\text{SiO}_5$  silicate: a perspective multifunctional thermal and environmental barrier coating material. *Scr Mater.* 2019;168:47–50. <https://doi.org/10.1016/j.scriptamat.2019.04.018>
  43. Chen H, Zhao Z, Xiang H, Dai F-Z, Xu W, Sun K, et al. High entropy ( $\text{Y}_{0.2}\text{Yb}_{0.2}\text{Lu}_{0.2}\text{Eu}_{0.2}\text{Er}_{0.2}$ ) $_3\text{Al}_5\text{O}_{12}$ : a novel high temperature stable thermal barrier material. *J Mater Sci Technol.* 2020;48:57–62. <https://doi.org/10.1016/j.jmst.2020.01.056>
  44. Zhao Z, Chen H, Xiang H, Dai F-Z, Wang X, Peng Z, et al. ( $\text{La}_{0.2}\text{Ce}_{0.2}\text{Nd}_{0.2}\text{Sm}_{0.2}\text{Eu}_{0.2}$ ) $\text{PO}_4$ : a high-entropy rare-earth phosphate monazite ceramic with low thermal conductivity and good compatibility with  $\text{Al}_2\text{O}_3$ . *J Mater Sci Technol.* 2019;35(12):2892–6. <https://doi.org/10.1016/j.jmst.2019.08.012>
  45. Vinnik DA, Trofimov EA, Zhivulin VE, Zaitseva OV, Zherebtsov DA, Starikov AY, et al. The new extremely substituted high entropy ( $\text{Ba,Sr,Ca,La}$ ) $\text{Fe}_{6x}$ ( $\text{Al,Ti,Cr,Ga,In,Cu,W}$ ) $_x\text{O}_{19}$  microcrystals with magnetoplumbite structure. *Ceram Int.* 2020;46(7):9656–60. <https://doi.org/10.1016/j.ceramint.2019.12.232>
  46. Chellali MR, Sarkar A, Nandam SH, Bhattacharya SS, Breitung B, Hahn H, et al. On the homogeneity of high entropy oxides: an investigation at the atomic scale. *Scr Mater.* 2019;166:58–63. <https://doi.org/10.1016/j.scriptamat.2019.02.039>
  47. Meisenheimer PB, Heron JT. Oxides and the high entropy regime: a new mix for engineering physical properties. *MRS Adv.* 2020;5:3419–3436. <https://doi.org/10.1557/adv.2020.295>
  48. Rost CM, Rak Z, Brenner DW, Maria J-P. Local structure of the  $\text{Mg}_x\text{Ni}_x\text{Co}_x\text{Cu}_x\text{Zn}_x\text{O}$  ( $x = 0.2$ ) entropy-stabilized oxide: an EXAFS study. *J Am Ceram Soc.* 2017;100(6):2732–8. <https://doi.org/10.1111/jace.14756>
  49. Rak Zs, Maria J-P, Brenner DW. Evidence for Jahn-Teller compression in the (Mg, Co, Ni, Cu, Zn)O entropy-stabilized oxide: a DFT study. *Mater Lett.* 2018;217:300–3. <https://doi.org/10.1016/j.matlet.2018.01.111>
  50. Berardan D, Meena AK, Franger S, Herrero C, Dragoe N. Controlled Jahn-Teller distortion in (MgCoNiCuZn)O-based high entropy oxides. *J Alloys Compd.* 2017;704:693–700. <https://doi.org/10.1016/j.jallcom.2017.02.070>
  51. Rak Z, Rost CM, Lim M, Sarker P, Toher C, Curtarolo S, et al. Charge compensation and electrostatic transferability in three entropy-stabilized oxides: results from density functional theory calculations. *J Appl Phys.* 2016;120(095105):095105. <https://doi.org/10.1063/1.4962135>
  52. Ranganathan S. Alloyed pleasures: multimetallic cocktails. *Curr Sci.* 2003;85(10):1404–6.
  53. Ophus C. Four-dimensional scanning transmission electron microscopy (4D-STEM): from scanning nanodiffraction to ptychography and beyond. *Microsc Microanal.* 2019;25:563–82. <https://doi.org/10.1017/S1431927619000497>
  54. Xu M, Kumar A, Lebeau JM. Towards augmented microscopy with reinforcement learning-enhanced workflows. *Microsc Microanal.* 2022;28(6):1952–60. <https://doi.org/10.1017/S1431927622012193>
  55. Xu M, Kumar A, LeBeau JM. Correlating local chemical and structural order using geographic information systems-based spatial statistics. *Ultramicroscopy.* 2023;243:113642. <https://doi.org/10.1016/J.ULTRAMIC.2022.113642>
  56. Fracchia M, Ghigna P, Pozzi T, Tamburini UA, Colombo V, Braglia L, et al. Stabilization by configurational entropy of the Cu(II) active site during CO oxidation on  $\text{Mg}_{0.2}\text{Co}_{0.2}\text{Ni}_{0.2}\text{Cu}_{0.2}\text{Zn}_{0.2}\text{O}$ . *J Phys Chem Lett.* 2020;11:3589–93. <https://doi.org/10.1021/acs.jpcclett.0c00602> PMID: 32309955
  57. Tavani F, Fracchia M, Pianta N, Ghigna P, Quartarone E, D'Angelo P. Multivariate curve resolution analysis of operando XAS data for the investigation of the lithiation mechanisms in high entropy oxides. *Chem Phys Lett.* 2020;760(August):137968. <https://doi.org/10.1016/j.cplett.2020.137968>
  58. Lun Z, Ouyang B, Kwon DH, Ha Y, Foley EE, Huang TY, et al. Cation-disordered rocksalt-type high-entropy cathodes for Li-ion batteries. *Nat Mater.* 2021;20:214–21. <https://doi.org/10.1038/s41563-020-00816-0> PMID: 33046857
  59. Achard FK. *Recherches Sur Les Propriétés Des Alliages Métalliques.* Berlin: Decker; 1788.
  60. Smith CS. *Four outstanding researchers in metallurgical history.* West Conshohocken: American Society for Testing and Materials; 1963.
  61. Chang X, Zeng M, Fu L. Phase engineering of high-entropy alloys. *Adv Mater.* 2020;32:1907226. <https://doi.org/10.1002/adma.201907226>



62. Senkov ON, Miracle DB, Chaput KJ, Couzinie JP. Development and exploration of refractory high entropy alloys—a review. *J Mater Res*. 2018;33(19):3092–128. <https://doi.org/10.1557/jmr.2018.153>
63. George EP, Raabe D, Ritchie RO. High-entropy alloys. *Nat Rev Mater*. 2019;4:515–34. <https://doi.org/10.1038/s41578-019-0121-4>
64. Chen T-K, Wong M-S. Structure and properties of reactively-sputtered  $\text{Al}_x\text{CoCrCuFeNi}$  oxide films. *Thin Solid Films*. 2007;516:141–6. <https://doi.org/10.1016/j.tsf.2007.06.142>
65. Bérardan D, Franger S, Meena AK, Dragoie N. Room temperature lithium superionic conductivity in high entropy oxides. *J Mater Chem A*. 2016;4(24):9536–41. <https://doi.org/10.1039/c6ta03249d>
66. Berardan D, Franger S, Dragoie D, Meena AK, Dragoie N. Colossal dielectric constant in high entropy oxides. *Phys Status Solidi – Rapid Res Lett*. 2016;10(4):328–33. <https://doi.org/10.1002/pssr.201600043>
67. Meisenheimer PB, Kratochvil TJ, Heron JT. Giant enhancement of exchange coupling in entropy-stabilized oxide heterostructures. *Sci Rep*. 2017;7:13344. <https://doi.org/10.1038/s41598-017-13810-5> PMID: 29042610
68. Anand G, Wynn AP, Handley CM, Freeman CL. Phase stability and distortion in high-entropy oxides. *Acta Mater*. 2018;146:119–25. <https://doi.org/10.1016/j.actamat.2017.12.037>
69. Sharma Y, Musico BL, Gao X, Hua C, May AF, Herklotz A, et al. Single-crystal high entropy perovskite oxide epitaxial films. *Phys Rev Mater*. 2018;2(6):60404. <https://doi.org/10.1103/PhysRevMaterials.2.060404>
70. Rost CM. Entropy-stabilized oxides: explorations of a novel class of multicomponent materials. Raleigh: North Carolina State University; 2016.
71. Chen K, Pei X, Tang L, Cheng H, Li Z, Li C, et al. A five-component entropy-stabilized fluorite oxide. *J Eur Ceram Soc*. 2018;38(11):4161–4. <https://doi.org/10.1016/j.jeurceramsoc.2018.04.063>
72. Zhai S, Rojas J, Ahlberg N, Lim K, Toney MF, Jin H, et al. The use of poly-cation oxides to lower the temperature of two-step thermochemical water splitting. *Energy Environ Sci*. 2018;11:2172–8. <https://doi.org/10.1039/c8ee00050f>
73. Chen H, Fu J, Zhang P, Peng H, Abney CW, Jie K, et al. Entropy-stabilized metal oxide solid solutions as CO oxidation catalysts with high-temperature stability. *J Mater Chem A*. 2018;6:11129–33. <https://doi.org/10.1039/c8ta01772g>
74. Yao Y, Dong Q, Brozena A, Luo J, Miao J, Chi M, et al. High-entropy nanoparticles: synthesis-structure property relationships and data-driven discovery. *Science*. 2022;376(6589). <https://doi.org/10.1126/science.abn3103>
75. Dupuy AD, Wang X, Schoenung JM. Entropic phase transformation in nanocrystalline high entropy oxides. *Mater Res Lett*. 2019;7(2):60–67. <https://doi.org/10.1080/21663831.2018.1554605>
76. Osenciat N, Berardan D, Dragoie D, Leridon B, Hole S, Meena AK, et al. Charge compensation mechanisms in Li-substituted high-entropy oxides and influence on Li superionic conductivity. *J Am Ceram Soc*. 2019;102:6156–62. <https://doi.org/10.1111/jace.16511>
77. Grzesik Z, Smoła G, Stygar M, Dąbrowa J, Zajusz M, Mroczka K, et al. Defect structure and transport properties in  $(\text{Co,Cu,Mg,Ni,Zn})\text{O}$  high entropy oxide. *J Eur Ceram Soc*. 2019;39(June):4292–8. <https://doi.org/10.1016/j.jeurceramsoc.2019.06.018>
78. Grzesik Z, Smoła G, Miszczak M, Stygar M, Dąbrowa J, Zajusz M, et al. Defect structure and transport properties of  $(\text{Co,Cr,Fe,Mn,Ni})_3\text{O}_4$  spinel-structured high entropy oxide. *J Eur Ceram Soc*. 2020;40(3):835–9. <https://doi.org/10.1016/j.jeurceramsoc.2019.10.026>
79. Zhang J, Yan J, Calder S, Zheng Q, McGuire MA, Abernathy DL, et al. Long-range antiferromagnetic order in a rocksalt high entropy oxide. *Chem Mater*. 2019;31(10):3705–11. <https://doi.org/10.1021/acs.chemmater.9b00624>
80. Rak Z, Brenner DW. Exchange interactions and long-range magnetic order in the  $(\text{Mg,Co,Cu,Ni,Zn})\text{O}$  entropy-stabilized oxide: a theoretical investigation. *J Appl Phys*. 2020;127:185108. <https://doi.org/10.1063/5.0008258>
81. Johnstone GHJ, González-Rivas MU, Taddei KM, Sutarto R, Sawatzky GA, Green RJ, et al. Entropy engineering and tunable magnetic order in the spinel high-entropy oxide. *J Am Chem Soc*. 2022;144(45):20590–600. <https://doi.org/10.1021/jacs.2c06768> PMID: 36321637
82. Mao A, Xiang HZ, Zhang ZG, Kuramoto K, Zhang H, Jia Y. A new class of spinel high-entropy oxides with controllable magnetic properties. *J Magn Magn Mater*. 2020;497:165884. <https://doi.org/10.1016/j.jmmm.2019.165884>
83. Zeng Y, Ouyang B, Liu J, Byeon YW, Cai Z, Miara LJ, et al. High-entropy mechanism to boost ionic conductivity. *Science*. 2022;378(6626):1320–4. <https://doi.org/10.1126/science.abq1346> PMID: 36548421
84. Pu Y, Zhang Q, Li R, Chen M, Du X, Zhou S. Dielectric properties and electrocaloric effect of high-entropy  $(\text{Na}_{0.2}\text{Bi}_{0.2}\text{Ba}_{0.2}\text{Sr}_{0.2}\text{Ca}_{0.2})\text{TiO}_3$  ceramic. *Appl Phys Lett*. 2019;115:223901. <https://doi.org/10.1063/1.5126652>
85. Liu J, Ren K, Ma C, Du H, Wang Y. Dielectric and energy storage properties of flash-sintered high-entropy  $(\text{Bi}_{0.2}\text{Na}_{0.2}\text{K}_{0.2}\text{Ba}_{0.2}\text{Ca}_{0.2})\text{TiO}_3$  ceramic. *Ceram Int*. 2020;56(12):20576–81. <https://doi.org/10.1016/j.ceramint.2020.05.090>
86. Xiong W, Zhang H, Cao S, Gao F, Svec P, Dusza J, et al. Low-loss high entropy relaxor-like ferroelectrics with A-site disorder. *J Eur Ceram Soc*. 2021;41(4):2979–85. <https://doi.org/10.1016/j.jeurceramsoc.2020.11.030>
87. Sharma Y, Lee MC, Pitike KC, Mishra KK, Zheng Q, Gao X, et al. High entropy oxide relaxor ferroelectrics. *ACS Appl Mater Interfaces*. 2022;14(9):11962–70. <https://doi.org/10.1021/acsami.2c00340> PMID: 35226475
88. Son Y, Zhu W, Trolrier-McKinstry SE. Electrocaloric effect of perovskite high entropy oxide films. *Adv Electron Mater*. 2022;8(12):1–9. <https://doi.org/10.1002/aelm.202200352>
89. Ushakov SV, Hayun S, Gong W, Navrotsky A. Thermal analysis of high entropy rare earth oxides. *Materials*. 2020;13(14):3141. <https://doi.org/10.3390/ma13143141> PMID: 32674493
90. Chen L, Wang Y, Hu M, Zhang L, Wang J, Zhang Z, et al. Achieved limit thermal conductivity and enhancements of mechanical properties in fluorite  $\text{RE}_3\text{NbO}_7$  via entropy engineering. *Appl Phys Lett*. 2021;118(7):071905. <https://doi.org/10.1063/5.0037373>
91. Ren K, Wang Q, Shao G, Zhao X, Wang Y. Multicomponent high-entropy zirconates with comprehensive properties for advanced thermal barrier coating. *Scr Mater*. 2020;178:382–6. <https://doi.org/10.1016/j.scriptamat.2019.12.006>
92. Wright AJ, Huang C, Walock MJ, Ghoshal A, Murugan M, Luo J. Sand corrosion, thermal expansion, and ablation of medium- and high-entropy compositionally complex fluorite oxides. *J*

- Am Ceram Soc. 2021;104(1):448–62. <https://doi.org/10.1111/jace.17448>
93. Zheng Y, Zou M, Zhang W, Yi D, Lan J, Nan CW, et al. Electrical and thermal transport behaviours of high-entropy perovskite thermoelectric oxides. *J Adv Ceram*. 2021;10(2):377–84. <https://doi.org/10.1007/s40145-021-0462-5>
  94. Zhang P, Lou Z, Gong L, Xu J, Chen Q, Reece MJ, et al. High-entropy MTiO<sub>3</sub> perovskite oxides with glass-like thermal conductivity for thermoelectric applications. *J Alloys Compd*. 2023;937:168366. <https://doi.org/10.1016/j.jallcom.2022.168366>
  95. Kinsler-Fedon C, Zheng Q, Huang Q, Choi ES, Yan J, Zhou H, et al. Synthesis, characterization, and single-crystal growth of a high-entropy rare-earth pyrochlore oxide. *Phys Rev Mater*. 2020;4(10):104411. <https://doi.org/10.1103/PhysRevMaterials.4.104411>
  96. Pianassola M, Loveday M, Chakoumakos BC, Koschan M, Melcher CL, Zhuravleva M. Crystal growth and elemental homogeneity of the multicomponent rare-earth garnet (Lu<sub>1/6</sub>Y<sub>1/6</sub>Ho<sub>1/6</sub>Dy<sub>1/6</sub>Tb<sub>1/6</sub>Gd<sub>1/6</sub>)<sub>3</sub>Al<sub>5</sub>O<sub>12</sub>. *Cryst Growth Des*. 2020;20(10):6769–76. <https://doi.org/10.1021/acs.cgd.0c00887>
  97. Wang B, Wang C, Yu X, Cao Y, Gao L, Wu C, et al. General synthesis of high-entropy alloy and ceramic nanoparticles in nanoseconds. *Nat Synth*. 2022;1(2):138–46. <https://doi.org/10.1038/s44160-021-00004-1>
  98. Li Y, Tay YY, Buenconsejo JS, Manalastas W, Tu WH, Lim HK, et al. Laser annealing-induced phase transformation behaviors of high entropy metal alloy, oxide, and nitride nanoparticle combinations. *Adv Funct Mater*. 2023;33:2211279. <https://doi.org/10.1002/ADFM.202211279>
  99. Stenzel D, Issac I, Wang K, Azmi R, Singh R, Jeong J, et al. High entropy and low symmetry: triclinic high-entropy molybdates. *Inorg Chem*. 2021;60(1):115–23. <https://doi.org/10.1021/acs.inorgchem.0c02501> PMID: 33314913
  100. DeHoff R. *Thermodynamics in materials science*. 2nd ed. Boca Raton, FL: Taylor & Francis; 2006.
  101. Xiang H-Z, Xie H-X, Mao A, Jia Y-G, Si T-Z. Facile preparation of single phase high-entropy oxide nanocrystalline powders by solution combustion synthesis. *Int J Mater*. 2020;111(3):246–9.
  102. Sarkar A, Eggert B, Velasco L, Mu X, Lill J, Ollefs K, et al. Role of intermediate 4f states in tuning the band structure of high entropy oxides. *Appl Phys Lett Mater*. 2020;8:051111. <https://doi.org/10.1063/5.0007944>
  103. Gorbenko OY, Samoilnikov SV, Graboy IE, Kaul AR. Epitaxial stabilization in thin films of oxides. *Chem Mater*. 2002;14(10):4026–43. <https://doi.org/10.1557/PROC-755-DD7.1>
  104. Kang ZC, Eyring LR. The structural basis of the fluorite-related rare earth higher oxides. *Aust J Chem*. 1996;49(9):981–96. <https://doi.org/10.1071/CH9960981>
  105. Coduri M, Scavini M, Allietta M, Brunelli M, Ferrero C. Defect structure of Y-doped ceria on different length scales. *Chem Mater*. 2013;25(21):4278–89. <https://doi.org/10.1021/cm402359d>
  106. Voskanyan AA, Lilova K, McCormack SJ, Kriven WM, Navrotsky A. A new class of entropy stabilized oxides: commensurately modulated A<sub>6</sub>B<sub>2</sub>O<sub>17</sub> (A = Zr, Hf; B = Nb, Ta) structures. *Scr Mater*. 2021;204. <https://doi.org/10.1016/J.SCRIPTAMAT.2021.114139>
  107. Palmer RG. Broken ergodicity. *Adv Phys*. 1982;31(6):669–735. <https://doi.org/10.1080/00018738200101438>
  108. Bhaskar LK, Nallathambi V, Kumar R. Critical role of cationic local stresses on the stabilization of entropy-stabilized transition metal oxides. *J Am Ceram Soc*. 2020;103:3416–24. <https://doi.org/10.1111/jace.17029>
  109. Chen J, Liu W, Liu J, Zhang X, Yuan M, Zhao Y, et al. Stability and compressibility of cation-doped high-entropy oxide MgCoNiCuZnO<sub>5</sub>. *J Phys Chem C*. 2019;123:17735–44. <https://doi.org/10.1021/acs.jpcc.9b04992>
  110. Mazza AR, Skoropata E, Lapano J, Zhang J, Sharma Y, Musico BL, et al. Charge doping effects on magnetic properties of single-crystal La<sub>1-x</sub>Sr<sub>x</sub>(Cr<sub>0.2</sub>Mn<sub>0.2</sub>Fe<sub>0.2</sub>Co<sub>0.2</sub>Ni<sub>0.2</sub>)O<sub>3</sub> (0 ≤ x ≤ 0.5) high-entropy perovskite oxides. *Phys Rev B*. 2021;104(9):094204. <https://doi.org/10.1103/PhysRevB.104.094204>
  111. Anandkumar M, Bagul PM, Deshpande AS. Structural and luminescent properties of Eu<sup>3+</sup> doped multi-principal component Ce<sub>0.2</sub>Gd<sub>0.2</sub>Hf<sub>0.2</sub>La<sub>0.2</sub>Zr<sub>0.2</sub>O<sub>2</sub> nanoparticles. *J Alloys Compd*. 2020;838:155595. <https://doi.org/10.1016/j.jallcom.2020.155595>
  112. Zhong Y, Sabarou H, Yan X, Yang M, Gao MC, Liu X, et al. Exploration of high entropy ceramics (HECs) with computational thermodynamics – a case study with LaMnO<sub>3±δ</sub>. *Mater Des*. 2019;182:108060. <https://doi.org/10.1016/j.matdes.2019.108060>
  113. Qiu N, Chen H, Yang Z, Sun S, Wang Y, Cui Y. A high entropy oxide (Mg<sub>0.2</sub>Co<sub>0.2</sub>Ni<sub>0.2</sub>Cu<sub>0.2</sub>Zn<sub>0.2</sub>O) with superior lithium storage performance. *J Alloys Compd*. 2019;777:767–74. <https://doi.org/10.1016/j.jallcom.2018.11.049>
  114. Chen H, Qiu N. Tunable pseudocapacitive contribution by dimension control in nanocrystalline-constructed (Mg<sub>0.2</sub>Co<sub>0.2</sub>Ni<sub>0.2</sub>Cu<sub>0.2</sub>Zn<sub>0.2</sub>)O solid solutions to achieve superior lithium-storage properties. *RCS Adv*. 2019;9:28908–15. <https://doi.org/10.1039/c9ra05508h>
  115. Zhang Y, Lu T, Ye Y, Dai W, Zhu Y, Pan Y. Stabilizing oxygen vacancy in entropy-engineered CoFe<sub>2</sub>O<sub>4</sub>-type catalysts for co-prosperity of efficiency and stability in an oxygen evolution reaction. *ACS Appl Mater Interfaces*. 2020;12(29):32548–55. <https://doi.org/10.1021/acsami.0c05916> PMID: 32614574
  116. Kotsonis GN, Meisenheimer PB, Miao L, Roth J, Wang B, Shafer P, et al. Property and cation valence engineering in entropy-stabilized oxide thin films. *Phys Rev Mater*. 2020;4(10):100401. <https://doi.org/10.1103/PhysRevMaterials.4.100401>
  117. Dąbrowa J, Szymczak M, Zajusz M, Mikuła A, Możdziej M, Berent K, et al. Stabilizing fluorite structure in ceria-based high-entropy oxides: influence of Mo addition on crystal structure and transport properties. *J Eur Ceram Soc*. 2020;40(15):5870–81. <https://doi.org/10.1016/j.jeurceramsoc.2020.07.014>
  118. Usharani NJ, Shringi R, Sanghavi H, Subramanian S, Bhattacharya SS. Role of size, alio-/multi-valency and non-stoichiometry in the synthesis of phase-pure high entropy oxide (Co,Cu,Mg,Na,Ni,Zn)O. *Dalton Trans*. 2020;49(21):7123–32. <https://doi.org/10.1039/d0dt00958j> PMID: 32406896
  119. Tang L, Li Z, Chen K, Li C, Zhang X, An L. High-entropy oxides based on valence combinations: design and practice. *J Am Ceram Soc*. 2021;104(5):1953–8. <https://doi.org/10.1111/jace.17659>
  120. Meisenheimer PB, Williams LD, Sung SH, Gim J, Shafer P, Kotsonis GN, et al. Magnetic frustration control through tunable stereochemically driven disorder in entropy-stabilized

- oxides. *Phys Rev Mater.* 2019;3:104420. <https://doi.org/10.1103/PhysRevMaterials.3.104420>
121. Brahlek M, Mazza AR, Pitike KC, Skoropata E, Lapano J, Eres G, et al. Unexpected crystalline homogeneity from the disordered bond network in  $\text{La}(\text{Cr}_{0.2}\text{Mn}_{0.2}\text{Fe}_{0.2}\text{Co}_{0.2}\text{Ni}_{0.2})\text{O}_3$  films. *Phys Rev Lett.* 2020;4:054407. <https://doi.org/10.1103/PhysRevMaterials.4.054407>
  122. Chae S, Williams L, Lee J, Heron JT, Kioupakis E. Effects of local compositional and structural disorder on vacancy formation in entropy-stabilized oxides from first-principles. *NPJ Comput Mater.* 2022;8(1). <https://doi.org/10.1038/s41524-022-00780-0>
  123. Liu J, Shao G, Liu D, Chen K, Wang K, Ma B, et al. Design and synthesis of chemically complex ceramics from the perspective of entropy. *Mater Today Adv.* 2020;8:100114. <https://doi.org/10.1016/j.mtadv.2020.100114>
  124. Sarker P, Harrington T, Toher C, Osos C, Samiee M, Maria J-P, et al. High-entropy high-hardness metal carbides discovered by entropy descriptors. *Nat Commun.* 2018;9:4980. <https://doi.org/10.1038/s41467-018-07160-7>
  125. Pitike KC, KC S, Eisenbach M, Bridges CA, Cooper VR. Predicting the phase stability of multicomponent high-entropy compounds. *Chem Mater.* 2020;32(17):7507–15. <https://doi.org/10.1021/acs.chemmater.0c02702>
  126. Gorsse S, Senkov ON. About the reliability of CALPHAD predictions in multicomponent systems. *Entropy.* 2018;20(12):899. <https://doi.org/10.3390/e20120899> PMID: 33266623
  127. Sharma A, Singh R, Liaw PK, Balasubramanian G. Cuckoo searching optimal composition of multicomponent alloys by molecular simulations. *Scr Mater.* 2017;130:292–6. <https://doi.org/10.1016/j.scriptamat.2016.12.022>
  128. Singh R, Sharma A, Singh P, Balasubramanian G, Johnson DD. Accelerating computational modeling and design of high-entropy alloys. *Nat Comput Sci.* 2021;1(1):54–61. <https://doi.org/10.1038/s43588-020-00006-7>
  129. Dai FZ, Wen B, Sun Y, Xiang H, Zhou Y. Theoretical prediction on thermal and mechanical properties of high entropy  $(\text{Zr}_{0.2}\text{Hf}_{0.2}\text{Ti}_{0.2}\text{Nb}_{0.2}\text{Ta}_{0.2})\text{C}$  by deep learning potential. *J Mater Sci Technol.* 2020;43:168–74. <https://doi.org/10.1016/j.jmst.2020.01.005>
  130. Pitike KC, Marquez-Rossy AE, Flores-Betancourt A, Chen DX, Santosh KC, Cooper VR, et al. On the elastic anisotropy of the entropy-stabilized oxide  $(\text{Mg}, \text{Co}, \text{Ni}, \text{Cu}, \text{Zn})\text{O}$  compound. *J Appl Phys.* 2020;128(1):015101. <https://doi.org/10.1063/5.0011352>
  131. Yoon B, Avila V, Raj R, Jesus LM. reactive flash sintering of the entropy-stabilized oxide  $\text{Mg}_{0.2}\text{Ni}_{0.2}\text{Co}_{0.2}\text{Cu}_{0.2}\text{Zn}_{0.2}\text{O}$ . *Scr Mater.* 2020;181(3):48–52. <https://doi.org/10.1016/j.scriptamat.2020.02.006>
  132. Liu D, Peng X, Liu J, Chen L, Yang Y, An L. Ultrafast synthesis of entropy-stabilized oxide at room temperature. *J Eur Ceram Soc.* 2020;40(6):2504–8. <https://doi.org/10.1016/j.jeurceramsoc.2020.01.018>
  133. Ma B, Zhu Y, Wang K, Sun Z, Ren K, Wang Y. Reactive flash sintering and electrical transport properties of high-entropy  $(\text{MgCoNiCuZn})_{1-x}\text{Li}_x\text{O}$  oxides. *J Am Ceram Soc.* 2022;105(6):3765–73. <https://doi.org/10.1111/jace.18343>
  134. Zhao Z, Chen H, Xiang H, Dai F-Z, Wang X, Xu W, et al. High-entropy  $(\text{Y}_{0.2}\text{Nd}_{0.2}\text{Sm}_{0.2}\text{Eu}_{0.2}\text{Er}_{0.2})\text{AlO}_3$ : a promising thermal/environmental barrier material for oxide/oxide composites. *J Mater Sci Technol.* 2020;47:45–51. <https://doi.org/10.1016/j.jmst.2020.02.011>
  135. Hong W, Chen F, Shen Q, Han Y-H, Fahrenholtz WG, Zhang L. Microstructural evolution and mechanical properties of  $(\text{Mg}, \text{Co}, \text{Ni}, \text{Cu}, \text{Zn})\text{O}$  high-entropy ceramics. *J Am Ceram Soc.* 2019;102(4):2228–37. <https://doi.org/10.1111/jace.16075>
  136. Tseng K-P, Yang Q, McCormack SJ, Kriven WM. High-entropy, phase-constrained lanthanide, sesquioxide. *J Am Ceram Soc.* 2020;103:569–576. <https://doi.org/10.1111/jace.16689>
  137. Chen H, Lin W, Zhang Z, Jie K, Mullins DR, Sang X, et al. Mechanochemical synthesis of high entropy oxide materials under ambient conditions: dispersion of catalysts via entropy maximization. *ACS Mater Lett.* 2019;1:83–8. <https://doi.org/10.1021/acsmaterialslett.9b00064>
  138. Musicó BL, Wright Q, Delzer C, Ward TZ, Rawn CJ, Mandrus DG, et al. Synthesis method comparison of compositionally complex rare earth-based Ruddlesden-Popper  $n = 1$  T'-type cuprates. *J Am Ceram Soc.* 2021;104(7):3750–9. <https://doi.org/10.1111/jace.17750>
  139. Radon A, Hawelek Ł, Łukowiec D, Kubacki J, Włodarczyk P. Dielectric and electromagnetic interference shielding properties of high entropy  $(\text{Zn}, \text{Fe}, \text{Ni}, \text{Mg}, \text{Cd})\text{Fe}_2\text{O}_4$  ferrite. *Sci Rep.* 2019;9:20078. <https://doi.org/10.1038/s41598-019-56586-6> PMID: 31882865
  140. Saghir AV, Beidokhti SM, Khaki JV, Salimi A. One-step synthesis of single-phase  $(\text{Co}, \text{Mg}, \text{Ni}, \text{Cu}, \text{Zn})\text{O}$  high entropy oxide nanoparticles through SCS procedure: thermodynamics and experimental evaluation. *J Eur Ceram Soc.* 2021;41(1):563–79. <https://doi.org/10.1016/j.jeurceramsoc.2020.08.044>
  141. Mao A, Xiang HZ, Zhang ZG, Kuramoto K, Yu H, Ran S. Solution combustion synthesis and magnetic property of rock-salt  $(\text{Co}_{0.2}\text{Cu}_{0.2}\text{Mg}_{0.2}\text{Ni}_{0.2}\text{Zn}_{0.2})\text{O}$  high-entropy oxide nanocrystalline powder. *J Magn Magn Mater.* 2019;484(March):245–52. <https://doi.org/10.1016/j.jmmm.2019.04.023>
  142. Biesuz M, Spiridigliozzi L, Dell'Agli G, Bortolotti M, Sglavo VM. Synthesis and sintering of  $(\text{Mg}, \text{Co}, \text{Ni}, \text{Cu}, \text{Zn})\text{O}$  entropy-stabilized oxides obtained by wet chemical methods. *J Mater Sci.* 2018;53(11):8074–85. <https://doi.org/10.1007/s10853-018-2168-9>
  143. Nguyen TX, Patra J, Chang JK, Ting JM. High entropy spinel oxide nanoparticles for superior lithiation-delithiation performance. *J Mater Chem A.* 2020;8(36):18963–73. <https://doi.org/10.1039/d0ta04844e>
  144. Dong Y, Ren K, Lu Y, Wang Q, Liu J, Wang Y. High-entropy environmental barrier coating for the ceramic matrix composites. *J Eur Ceram Soc.* 2019;39(7):2574–9. <https://doi.org/10.1016/j.jeurceramsoc.2019.02.022>
  145. Parida T, Karati A, Guruvadyathri K, Murty BS, Markandeyulu G. Novel rare-earth and transition metal-based entropy stabilized oxides with spinel structure. *Scr Mater.* 2020;178:513–7. <https://doi.org/10.1016/j.scriptamat.2019.12.027>
  146. Tang X, Hu L, Zhu X, Zhu X, Wang Y, Sun Y. Orientations-dependent metal-to-insulator transition in solution-deposited high-entropy nickelate thin films. *Cryst Growth Des.* 2022;22(12):7317–24. <https://doi.org/10.1021/acs.cgd.2c00945>
  147. Okejiri F, Zhang Z, Liu J, Liu M, Yang S, Dai S. Room-temperature synthesis of high-entropy perovskite oxide nanoparticle catalysts through ultrasonication-based method.



- ChemSusChem. 2020;13:111–5. <https://doi.org/10.1002/cssc.201902705> PMID: 31721472
148. Sarkar A, Djenadic R, Usharani NJ, Sanghvi KP, Chakravadhanula VSK, Gandhi AS, et al. Nanocrystalline multicomponent entropy stabilised transition metal oxides. *J Eur Ceram Soc.* 2017;37(2):747–54. <https://doi.org/10.1016/j.jeurceramsoc.2016.09.018>
  149. Sharma Y, Zheng Q, Mazza AR, Skoropata E, Heitmann T, Gai Z, et al. Magnetic anisotropy in single-crystal high-entropy perovskite oxide  $\text{La}(\text{Cr}_{0.2}\text{Mn}_{0.2}\text{Fe}_{0.2}\text{Co}_{0.2}\text{Ni}_{0.2})\text{O}_3$  films. *Phys Rev Mater.* 2020;4(1):14404. <https://doi.org/10.1103/PhysRevMaterials.4.014404>
  150. Zhang W, Mazza AR, Skoropata E, Mukherjee D, Musico B, Zhang J, et al. Applying configurational complexity to the 2D Ruddlesden-Popper crystal structure. *ACS Nano.* 2020;14(10):13030–7. <https://doi.org/10.1021/acsnano.0c04487> PMID: 32931257
  151. Sharma Y, Mazza AR, Musico BL, Skoropata E, Nepal R, Jin R, et al. Magnetic texture in insulating single crystal high entropy oxide spinel films. *ACS Appl Mater Interfaces.* 2021;13:17971–7. <https://doi.org/10.1021/acsaami.1c01344> PMID: 33822581
  152. Jacobson V, Diercks D, To B, Zakutayev A, Brennecke G. Thin film growth effects on electrical conductivity in entropy stabilized oxides. *J Eur Ceram Soc.* 2020;41:2617–24. <https://doi.org/10.1016/j.jeurceramsoc.2020.12.021>
  153. Kirnbauer A, Spadt C, Koller CM, Kolozsvari S, Mayrhofer PH. High-entropy oxide thin films based on Al–Cr–Nb–Ta–Ti. *Vacuum.* 2019;168:108850. <https://doi.org/10.1016/j.vacuum.2019.108850>
  154. Nguyen TX, Su YH, Hattrick-Simpers J, Joress H, Nagata T, Chang KS, et al. Exploring the first high-entropy thin film libraries: composition spread-controlled crystalline structure. *ACS Comb Sci.* 2020;22:858–66. <https://doi.org/10.1021/acscmbosci.0c00159> PMID: 33146510
  155. Yao Y, Dong Q, Brozena A, Luo J, Miao J, Chi M, et al. High-entropy nanoparticles: synthesis-structure property relationships and data-driven discovery. *Science.* 2022;376(6589). <https://doi.org/10.1126/science.abn3103>
  156. Botros M, Janek J. Embracing disorder in solid-state batteries. *Science.* 2022;378(6626):1273–1274. PMID: 36548419. <https://doi.org/10.1126/science.adf3383>
  157. Lokcu E, Toparli C, Anik M. Electrochemical performance of  $(\text{MgCoNiZn})_{1-x}\text{Li}_x\text{O}$  high-entropy oxides in lithium-ion batteries. *ACS Appl Mater Interfaces.* 2020;12:23860–6. <https://doi.org/10.1021/acsaami.0c03562> PMID: 32368889
  158. Wang Q, Sarkar A, Li Z, Lu Y, Velasco L, Bhattacharya SS, et al. High entropy oxides as anode material for Li-ion battery applications: a practical approach. *Electrochem Commun.* 2019;100:121–5. <https://doi.org/10.1016/j.elecom.2019.02.001>
  159. Ghigna P, Airolidi L, Fracchia M, Callegari D, Anselmi-Tamburini U, D'angelo P, et al. Lithiation mechanism in high-entropy oxides as anode materials for Li-ion batteries: an operando XAS study. *ACS Appl Mater Interfaces.* 2020;12(45):50344–54. <https://doi.org/10.1021/acsaami.0c13161> PMID: 33124794
  160. Chen H, Qiu N, Wu B, Yang Z, Sun S, Wang Y. A new spinel high-entropy oxide  $(\text{Mg}_{0.2}\text{Ti}_{0.2}\text{Zn}_{0.2}\text{Cu}_{0.2}\text{Fe}_{0.2})_3\text{O}_4$  with fast reaction kinetics and excellent stability as an anode material for lithium ion batteries. *RSC Adv.* 2020;10(16):9736–44. <https://doi.org/10.1039/d0ra00255k> PMID: 35497245
  161. Wang D, Jiang S, Duan C, Mao J, Dong Y, Dong K, et al. Spinel-structured high entropy oxide  $(\text{FeCoNiCrMn})_3\text{O}_4$  as anode towards superior lithium storage performance. *J Alloys Compd.* 2020;844:156158. <https://doi.org/10.1016/j.jallcom.2020.156158>
  162. Wang Q, Sarkar A, Wang D, Velasco L, Azmi R, Bhattacharya SS, et al. Multi-anionic and -cationic compounds: new high entropy materials for advanced Li-ion batteries. *Energy Environ Sci.* 2019;12:2433. <https://doi.org/10.1039/C9EE00368A>
  163. Wang J, Cui Y, Wang Q, Wang K, Huang X, Stenzel D, et al. Lithium containing layered high entropy oxide structures. *Sci Rep.* 2020;10(1):18430. <https://doi.org/10.1038/s41598-020-75134-1> PMID: 33116224
  164. Zhao C, Ding F, Lu Y, Chen L, Hu Y-S. High-entropy layered oxide cathodes for sodium-ion batteries. *Angew Chem.* 2020;59:264–9. <https://doi.org/10.1002/anie.201912171>
  165. Dąbrowa J, Olszewska A, Falkenstein A, Schwab C, Szymczak M, Zajusz M, et al. An innovative approach to design SOFC air electrode materials: high entropy  $\text{La}_{1-x}\text{Sr}_x(\text{Co,Cr,Fe,Mn,Ni})\text{O}_{3-\delta}$  ( $x = 0, 0.1, 0.2, 0.3$ ) perovskites synthesized by the sol-gel method. *J Mater Chem A.* 2020;8:24455–68. <https://doi.org/10.1039/d0ta06356h>
  166. Yang Y, Bao H, Ni H, Ou X, Wang S, Lin B, et al. A novel facile strategy to suppress Sr segregation for high-entropy stabilized  $\text{La}_{0.8}\text{Sr}_{0.2}\text{MnO}_{3-\delta}$  cathode. *J Power Sources.* 2021;482:228959. <https://doi.org/10.1016/j.jpowsour.2020.228959>
  167. Han X, Yang Y, Fan Y, Ni H, Guo Y, Chen Y, et al. New approach to enhance Sr-free cathode performance by high-entropy multi-component transition metal coupling. *Ceram Int.* 2021;47(12):17383–90. <https://doi.org/10.1016/j.ceramint.2021.03.052>
  168. Zheng Y, Yi Y, Fan M, Liu H, Li X, Zhang R, et al. A high-entropy metal oxide as chemical anchor of polysulfide for lithium-sulfur batteries. *Energy Storage Mater.* 2019;23:678–83. <https://doi.org/10.1016/j.ensm.2019.02.030>
  169. Li T, Yao Y, Huang Z, Xie P, Liu Z, Yang M, et al. Denary oxide nanoparticles as highly stable catalysts for methane combustion. *Nat Catal.* 2021;4(1):62–70. <https://doi.org/10.1038/s41929-020-00554-1>
  170. Zhivulin VE, Trofimov EA, Gudkova SA, Pashkeev IY, Punda AY, Gavriljak M, et al. Polysubstituted high-entropy  $[\text{LaNd}](\text{Cr}_{0.2}\text{Mn}_{0.2}\text{Fe}_{0.2}\text{Co}_{0.2}\text{Ni}_{0.2})\text{O}_3$  perovskites: correlation of the electrical and magnetic properties. *Nanomaterials.* 2021;11:1014. PMID: 33921115. <https://doi.org/10.3390/nano11041014>
  171. Sarkar A, Eggert B, Witte R, Lill J, Velasco L, Wang Q, et al. Comprehensive investigation of crystallographic, spin-electronic and magnetic structure of  $(\text{Co}_{0.2}\text{Cr}_{0.2}\text{Fe}_{0.2}\text{Mn}_{0.2}\text{Ni}_{0.2})_3\text{O}_4$ : unraveling the suppression of configuration entropy in high entropy oxides. *Acta Mater.* 2022;226:117581. <https://doi.org/10.1016/j.actamat.2021.117581>
  172. Witte R, Sarkar A, Velasco L, Kruk R, Brand RA, Eggert B, et al. Magnetic properties of rare-earth and transition metal based perovskite type high entropy oxides. *J Appl Phys.* 2020;127(18):185109. <https://doi.org/10.1063/5.0004125>
  173. Min L, Sretenovic M, Heitmann TW, Valentine TW, Zu R, Gopalan V, et al. A topological kagome magnet in high entropy



- form. *Commun Phys.* 2022;5(1):1–7. <https://doi.org/10.1038/s42005-022-00842-1>
174. Mazza AR, Skoropata E, Sharma Y, Lapano J, Heitmann TW, Musico BL, et al. Designing magnetism in high entropy oxides. *Adv Sci.* 2022;9(10):2200391. <https://doi.org/10.1002/advs.202200391>
  175. Farhan A, Stramaglia F, Cocconcetti M, Kuznetsov N, Yao L, Kleibert A, et al. Weak ferromagnetism in Tb (Fe<sub>0.2</sub>Mn<sub>0.2</sub>Co<sub>0.2</sub>Cr<sub>0.2</sub>Ni<sub>0.2</sub>)O<sub>3</sub> high-entropy oxide perovskite thin films. *Phys Rev B.* 2022;106(6):L060404. <https://doi.org/10.1103/PhysRevB.106.L060404>
  176. Bhattacharya A, May SJ. Magnetic oxide heterostructures. *Annu Rev Mater Res.* 2014;44(1):65–90. <https://doi.org/10.1146/annurev-matsci-070813-113447>
  177. Moździerz M, Dąbrowa J, Stępień A, Zajusz M, Stygar M, Zając W, et al. Mixed ionic-electronic transport in the high-entropy (Co,Cu,Mg,Ni,Zn)<sub>1-x</sub>Li<sub>x</sub>O oxides. *Acta Mater.* 2021;208:116735. <https://doi.org/10.1016/j.actamat.2021.116735>
  178. Gazda M, Miruszewski T, Jaworski D, Mielewczyk-Gryń A, Skubida W, Wachowski S, et al. Novel class of proton conducting materials – high entropy oxides. *ACS Mater Lett.* 2020;2(10):1315–21. <https://doi.org/10.1021/acsmaterialslett.0c00257>
  179. Bonnet E, Grenier JC, Bassat JM, Jacob A, Delatouche B, Bourdais S. On the ionic conductivity of some zirconia-derived high-entropy oxides. *J Eur Ceram Soc.* 2021;41(8):4505–15. <https://doi.org/10.1016/j.jeurceramsoc.2021.03.021>
  180. Wang K, Hou Q, Pal A, Wu H, Si J, Chen J, et al. Structural and physical properties of high-entropy REBa<sub>2</sub>Cu<sub>3</sub>O<sub>7-δ</sub> oxide superconductors. *J Supercond Nov Magn.* 2021;34(5):1379–85. <https://doi.org/10.1007/s10948-021-05855-5>
  181. Krawczyk PA, Jurczyszyn M, Pawlak J, Salamon W, Baran P, Kmita A, et al. High-entropy perovskites as multifunctional metal oxide semiconductors: synthesis and characterization of (Gd<sub>0.2</sub>Nd<sub>0.2</sub>La<sub>0.2</sub>Sm<sub>0.2</sub>Y<sub>0.2</sub>)CoO<sub>3</sub>. *ACS Appl Electron Mater.* 2020;2(10):3211–20. <https://doi.org/10.1021/acsaelm.0c00559> PMID: 33196046
  182. Sarkar A, Wang D, Kante MV, Eiselt L, Trouillet V, Iankevich G, et al. High entropy approach to engineer strongly correlated functionalities in manganites. *Adv Mater.* 2023;35(2):2207436. <https://doi.org/10.1002/adma.202207436>
  183. Zhou S, Pu Y, Zhang Q, Shi R, Guo X, Wang W, et al. Microstructure and dielectric properties of high entropy Ba(Zr<sub>0.2</sub>Ti<sub>0.2</sub>Sn<sub>0.2</sub>Hf<sub>0.2</sub>Me<sub>0.2</sub>)O<sub>3</sub> perovskite oxides. *Ceram Int.* 2020;46(6):7430–7. <https://doi.org/10.1016/j.ceramint.2019.11.239>
  184. Liu Z, Xu S, Li T, Xie B, Guo K, Lu J. Microstructure and ferroelectric properties of high-entropy perovskite oxides with A-site disorder. *Ceram Int.* 2021;47(23):33039–46. <https://doi.org/10.1016/j.ceramint.2021.08.204>
  185. Zhang M, Xu X, Yue Y, Palma M, Reece MJ, Yan H. Multi elements substituted Aurivillius phase relaxor ferroelectrics using high entropy design concept. *Mater Des.* 2021;200:109447. <https://doi.org/10.1016/j.matdes.2020.109447>
  186. Chen YW, Ruan JJ, Ting JM, Su YH, Chang KS. Solution-based fabrication of high-entropy Ba(Ti,Hf,Zr,Fe,Sn)O<sub>3</sub> films on fluorine-doped tin oxide substrates and their piezoelectric responses. *Ceram Int.* 2021;47(8):11451–8. <https://doi.org/10.1016/j.ceramint.2020.12.272>
  187. Scott JF. Electrocaloric materials. *Annu Rev Mater Res.* 2011;41:229–40. <https://doi.org/10.1146/annurev-matsci-062910-100341>
  188. Heitmann AA, Rossetti GA Jr. Thermodynamics of ferroelectric solid solutions with morphotropic phase boundaries. *J Am Ceram Soc.* 2014;97(6):1661–85. <https://doi.org/10.1111/jace.12979>
  189. Sarkar A, Mannava PK, Velasco L, Das C, Breitung B, Bhattacharya SS, et al. Determining role of individual cations in high entropy oxides: structure and reversible tuning of optical properties. *Scr Mater.* 2022;207:114273. <https://doi.org/10.1016/j.scriptamat.2021.114273>
  190. Karati A, Parida T, Gupta J, Adigilli HK, Borse PH, Joardar J. Band-gap engineering in novel delafossite-type multicomponent oxides for photocatalytic degradation of methylene blue. *Mater Res Bull.* 2021;137:111181. <https://doi.org/10.1016/j.materresbull.2020.111181>
  191. Edalati P, Wang Q, Razavi-Khosroshahi H, Fuji M, Ishihara T, Edalati K. Photocatalytic hydrogen evolution on a high-entropy oxide. *J Mater Chem A.* 2020;8(7):3814–21. <https://doi.org/10.1039/c9ta12846h>
  192. Zhang G, Milisavljevic I, Grzeszkiewicz K, Stachowiak P, Hreniak D, Wu Y. New optical ceramics: high-entropy sesquioxide X<sub>2</sub>O<sub>3</sub> multi-wavelength emission phosphor transparent ceramics. *J Eur Ceram Soc.* 2021;41(6):3621–8. <https://doi.org/10.1016/j.jeurceramsoc.2021.01.027>
  193. Zhang X, Li Y, Li C, Yang F, Jiang Z, Xue L, et al. A novel (La<sub>0.2</sub>Ce<sub>0.2</sub>Gd<sub>0.2</sub>Er<sub>0.2</sub>Tm<sub>0.2</sub>)<sub>2</sub>(WO<sub>4</sub>)<sub>3</sub> high-entropy ceramic material for thermal neutron and gamma-ray shielding. *Mater Des.* 2021;205:109722. <https://doi.org/10.1016/j.matdes.2021.109722>
  194. Zhou L, Li F, Liu JX, Sun SK, Liang Y, Zhang GJ. High-entropy A<sub>2</sub>B<sub>2</sub>O<sub>7</sub>-type oxide ceramics: a potential immobilising matrix for high-level radioactive waste. *J Hazard Mater.* 2021;415:125596. <https://doi.org/10.1016/j.jhazmat.2021.125596> PMID: 33725552
  195. Cheng B, Lou H, Sarkar A, Zeng Z, Zhang F, Chen X, et al. Lattice distortion and stability of (Co<sub>0.2</sub>Cu<sub>0.2</sub>Mg<sub>0.2</sub>Ni<sub>0.2</sub>Zn<sub>0.2</sub>)O high-entropy oxide under high pressure. *Mater Today Adv.* 2020;8:100102. <https://doi.org/10.1016/j.mtadv.2020.100102>
  196. Cheng B, Lou H, Sarkar A, Zeng Z, Zhang F, Chen X, et al. Pressure-induced tuning of lattice distortion in a high-entropy oxide. *Commun Chem.* 2019;2:114. <https://doi.org/10.1038/s42004-019-0216-2>

**How to cite this article:** Kotsonis GN, Almishal SSI, Marques dos Santos Vieira F, Crespi VH, Dabo I, Rost CM, et al. High-entropy oxides: Harnessing crystalline disorder for emergent functionality. *J Am Ceram Soc.* 2023;106:5587–5611. <https://doi.org/10.1111/jace.19252>